Surface enhancements, hydrophobicity, and gravitational effects on filmwise and dropwise flow condensation heat transfer for steam in mini-channels

by

Gennifer Anne Riley

B.S., Kansas State University, 2017
B.S., Washburn University, 2017

AN ABSTRACT OF A DISSERTATION

submitted in partial fulfillment of the requirements for the degree

DOCTOR OF PHILOSOPHY

Alan Levin Department of Mechanical and Nuclear Engineering
Carl R. Ice College of Engineering

KANSAS STATE UNIVERSITY
Manhattan, Kansas

2023

Abstract

Condensation heat transfer is an important part of thermal management systems, which take advantage of the latent heat of a two-phase working fluid. The main thermal resistance of filmwise condensation is the liquid film near the condensing surface, and reducing the liquid film thickness enhances condensation heat transfer due to the decreased thermal resistance. This dissertation investigates the effects of hemispherical mounds, porous surfaces, and hydrophobicity on forced condensation heat transfer in micro-channels. Also investigated were the impacts that spatial orientation of the three-sided condensation surface (i.e., gravitational effects) on steam flow condensation, where the cooled surfaces were either the lower surface (i.e., gravity pulls liquid towards the condensing surfaces) or upper surface (i.e., gravity pulls liquid away from the condensing surfaces).

A total of five copper test coupons were used, all with 1.9-mm hydraulic diameters for the condensing flows A plain, unmodified, flat surface was used as a control against which to compare the other coupons. Two coupons had a porous monolayer made of 100 μm or 200 μm copper particles. An additional two coupons were modified to have 16, 2-mm diameter hemispheres which were either solid copper or made of 200 μm copper particles. After the initial experiments, the plain coupon was coated in Teflon AF to become hydrophobic (i.e., contact angle approximately 110^{o}). Heat transfer coefficients, film visualization, and pressure drop measurements were recorded for each coupon at mass fluxes of 50 kg/m^2s and 125 kg/m^2s. The plain, both hydrophilic and hydrophobic, and solid mound coupons were tested in both the standard and inverted orientations.

Compared to the plain hydrophilic coupon in standard orientation, the solid mound coupon was found to increase the heat transfer coefficients by 13% to 79%, with the greatest increases

occurring at low qualities ($x < 0.4$) or high qualities ($x > 0.6$). The sintered mound coupon performed similarly to the solid mound coupon, though with generally less enhancement. Flow visualization suggests that the mounds enhanced heat transfer due to the disruption of the condensate film as well as by reducing the thermal resistance of the film. In the monolayer coupons, both saw modest, less than 20%, heat transfer coefficient enhancement in the mass flux of 125 kg/m^{2}s case, while for 50 kg/m^{2}s, both monolayer coupons had points where the heat transfer coefficient was reduced by up to 10%.

When the plain and solid mound test sections were inverted (i.e., condensing surface on the top of flowing steam), minimal differences were found in mound heat transfer performance, while the plain coupon reduces heat transfer coefficients by as much as 14%. The most significant enhancements and condensation mechanism changes occurred for the hydrophobic plain coupon. In the standard orientation, heat transfer coefficients were enhanced by up to 656% and in the inverted case, the enhancement increased by up to 987% compared to the hydrophilic coupon. Visualization showed that in the hydrophobic case, dropwise condensation was occurring. However, no condensation was observed on the inverted hydrophobic surface, likely due to the small size of the condensing droplets; a droplet forces analysis is included which supports decreased droplet size for the inverted, hydrophobic case. Heat transfer coefficient enhancements for low quality ($x < 0.4$) and low mass fluxes ($G = 50$ kg/m^{2}s) in the inverted hydrophobic plain coupon and in the hydrophilic solid mound coupon are of particular note, as these conditions provide lower heat transfer coefficients in simple condensers.

Surface enhancements, hydrophobicity, and gravitational effects on filmwise and dropwise flow condensation heat transfer for steam in mini-channels

by

Gennifer Anne Riley

B.S., Kansas State University, 2017
B.S., Washburn University, 2017

A DISSERTATION

submitted in partial fulfillment of the requirements for the degree

DOCTOR OF PHILOSOPHY

Alan Levin Department of Mechanical and Nuclear Engineering
Carl R. Ice College of Engineering

KANSAS STATE UNIVERSITY
Manhattan, Kansas

2023

Approved by:

Major Professor
Dr. Melanie M. Derby

Copyright

Abstract

Condensation heat transfer is an important part of thermal management systems, which take advantage of the latent heat of a two-phase working fluid. The main thermal resistance of filmwise condensation is the liquid film near the condensing surface, and reducing the liquid film thickness enhances condensation heat transfer due to the decreased thermal resistance. This dissertation investigates the effects of hemispherical mounds, porous surfaces, and hydrophobicity on forced condensation heat transfer in micro-channels. Also investigated were the impacts that spatial orientation of the three-sided condensation surface (i.e., gravitational effects) on steam flow condensation, where the cooled surfaces were either the lower surface (i.e., gravity pulls liquid towards the condensing surfaces) or upper surface (i.e., gravity pulls liquid away from the condensing surfaces).

A total of five copper test coupons were used, all with 1.9-mm hydraulic diameters for the condensing flows A plain, unmodified, flat surface was used as a control against which to compare the other coupons. Two coupons had a porous monolayer made of 100 μm or 200 μm copper particles. An additional two coupons were modified to have 16, 2-mm diameter hemispheres which were either solid copper or made of 200 μm copper particles. After the initial experiments, the plain coupon was coated in Teflon AF to become hydrophobic (i.e., contact angle approximately 110^{o}). Heat transfer coefficients, film visualization, and pressure drop measurements were recorded for each coupon at mass fluxes of 50 kg/m^2s and 125 kg/m^2s. The plain, both hydrophilic and hydrophobic, and solid mound coupons were tested in both the standard and inverted orientations.

Compared to the plain hydrophilic coupon in standard orientation, the solid mound coupon was found to increase the heat transfer coefficients by 13% to 79%, with the greatest increases

occurring at low qualities ($x < 0.4$) or high qualities ($x > 0.6$). The sintered mound coupon performed similarly to the solid mound coupon, though with generally less enhancement. Flow visualization suggests that the mounds enhanced heat transfer due to the disruption of the condensate film as well as by reducing the thermal resistance of the film. In the monolayer coupons, both saw modest, less than 20%, heat transfer coefficient enhancement in the mass flux of 125 kg/m^{2}s case, while for 50 kg/m^{2}s, both monolayer coupons had points where the heat transfer coefficient was reduced by up to 10%.

When the plain and solid mound test sections were inverted (i.e., condensing surface on the top of flowing steam), minimal differences were found in mound heat transfer performance, while the plain coupon reduces heat transfer coefficients by as much as 14%. The most significant enhancements and condensation mechanism changes occurred for the hydrophobic plain coupon. In the standard orientation, heat transfer coefficients were enhanced by up to 656% and in the inverted case, the enhancement increased by up to 987% compared to the hydrophilic coupon. Visualization showed that in the hydrophobic case, dropwise condensation was occurring. However, no condensation was observed on the inverted hydrophobic surface, likely due to the small size of the condensing droplets; a droplet forces analysis is included which supports decreased droplet size for the inverted, hydrophobic case. Heat transfer coefficient enhancements for low quality ($x < 0.4$) and low mass fluxes ($G = 50$ kg/m^{2}s) in the inverted hydrophobic plain coupon and in the hydrophilic solid mound coupon are of particular note, as these conditions provide lower heat transfer coefficients in simple condensers.

Table of Contents

List of Figures

List of Tables

Acknowledgements

My thanks and appreciation to all of those who have helped guide me through graduate school, particularly my advisor Dr. Melanie Derby, whose knowledge, patience, and wisdom made reaching this point possible. To the other members of my committee: Dr. Eckels, Dr. Betz, and Dr. Parameswaran, whose time, effort, and perspectives have helped me become a more well-rounded researcher. And to Dr. Hwang, who led the collaborative research project that got me started down this road. For their assistance in data collection, I thank Nicole Doughramaji, David Navarrete, and David Mendez. For providing me with comradery both as fellow graduate students and friends, I thank my fellow members of CHIL whose company was always sure to improve the course of my day.

For their financial support, I thank the NASA Cooperative Agreement Notice, Grant Number 80NSSC18M0030 for the primary support of the project, and the NSF Grant Number 1651451.

Dedication

Dedicated to wonderful spouse, Olivia Riley, who has been there with me through all the highs and lows of completing my education with love, support, and patience. Also, my cats; Jakoby and Freya because they are cute and fluffy.

Preface

Portions of Chapters 1-5 as well as Figures 3.1, 3.2, 3.4, 3.5, 4.2, 4.7, 4.8, 4.9, 5.1, 5.2, 5.4, and 5.5 in this dissertation are from the paper:

[1] G. A. Riley, C. E. Mendez, M. Egbo, G. Hwang, and M. M. Derby, "Visualizing and disrupting liquid films for filmwise flow condensation in horizontal minichannels," *Frontiers in Thermal Engineering*, vol. 2, p. 953051, 2022.

Chapter - 1 Introduction

Closed-loop thermal management systems utilize their working fluid to remove heat from a source, such as electronics or motors, and reject that heat into a heat sink, such as a radiator [2]. In space, it is particularly important to be able to move the thermal energy since cooling of the entire system is only possible by thermal radiation [3, 4]. By using a two-phase fluid in the closed-loop, the latent heat of the working fluid can be used advantageously by either evaporating or condensing it, allowing for significant heat transfer without significant temperature gradients in the fluid. While microgravity presents challenges to both condensing and boiling heat transfer, the heat transfer coefficients and enhancements for condensing tend to be lower than that of boiling, making improvements in condensation vital to improving thermal management systems [3, 4]. Reducing the mass and increasing the load that the thermal management system is capable of handling of, which is of particular interest as the costs of launching into low Earth orbit is on the order of 3000$/kg [5].

For condensation processes, the condensed liquid (i.e., condensate) acts to insulate the cooling surface from the working fluid [6-8]. While condensation can be dropwise or filmwise, filmwise condensation is prevalent in internal flows as it does not require any special coatings or conditions to occur [8-10]. Since the film in filmwise condensation prevents direct heat transfer between the cooling surface and the vapor, heat transfer coefficients tend to be an order of magnitude lower compared to dropwise condensation [11-13]. In order to enhance filmwise condensation heat transfer coefficients, a variety of methods have been analyzed including but not limited to decreasing the hydraulic diameter, increasing mass flux, the addition of structures in the channel, and evaluating the fluids with different properties such as surface tension and saturation temperature [2, 14, 15]. Significant room for studying the heat transfer coefficients of steam in

mini-channels exists within the literature, particularly in regard to the addition of structures and micro-gravitational effects. As such, this dissertation focuses on measuring steam condensation, sections 3-4.1, analyzing the effects of surface structures, sections 4.2-4.4, surface orientation, Chapter 5, and surface hydrophobicity, Chapter 6, on steam flow condensation such that lighter, less power demanding thermal management systems can be designed for application space applications.

Chapter - 2 Literature review

When a condensable fluid, such as steam, is flowing through a cooled channel, condensate will form on the channel wall. The condensate on the surface will increase the thermal resistance and reduce the rate of heat exchange [2, 12, 14, 16-18]. However, the shear forces from the working fluid passing over the condensate will act to thin or clear the surface of condensate while also condensing further itself [17, 19-23]. If the condensate is not cleared from the cooling surface quickly enough, then it will begin to form a film over the entire condensing surface, in a process called filmwise condensation. Should the condensate droplets instead be removed from the surface before a film is formed, dropwise condensation will occur. The condensation mode and heat transfer properties for a given condensing system are determined by the surface and geometric properties of the channel (i.e. the hydraulic diameter, hydrophobicity, and surface structure) as well as the two-phase quality, mass flux, and other properties of the working fluid [2, 12-15, 17, 18, 24-27].

2.1 Flow condensation in mini-channels

Since the convective heat transfer rate is a function of surface area, smaller channels, where the relative ratio of surface area to cross sectional area is higher and the vapor exerts increased shear forces on the film, offer greater heat transfer coefficients than larger channels [12, 14, 17, 18]. As channel size decreases, gravitation forces also decrease relative to buoyant, adhesive, and shear forces within the channel, causing different condensate flow regimes development than what is often seen in larger channels (e.g., hydraulic diameter > 3 mm) where the effects of gravity pull the condensate into a stratified layer at the bottom of the channel [21, 22, 28]. For filmwise condensation in mini-channels, where the hydraulic diameter is between 200 μm and 3 mm, the condensate film that develops will tend toward forming an annulus covering the entire inner

perimeter of the channel and direct condensation of the vapor onto the cooling surface or condensate film [20, 21, 28, 29].

While the presence of a liquid barrier between the vapor phase and the cooling surface increases thermal resistance, shear forces from the flowing vapor core prevent the annulus of condensation from remaining stationary. This movement allows for convective heat transfer to occur between it and the wall, preventing a worst-case-scenario for the thermal resistance where only conductive heat transfer is occurring through the film [30-33]. However, as the flow progresses through the channel and continues to condense, the quality of the steam and the velocity of the vapor core both decrease causing convection through the film to decrease and for other flow regimes to develop until the fluid has fully condensed [14, 17, 34-37].

2.2 Filmwise flow regimes in mini-channels

While in mini-channels, the condensate film will tend to wet the entire surface, forming an annulus of condensate through which the remaining vapor flows, annular flow is not the only flow regime that can occur [38-40]. Kim et. al. [19, 20] evaluated and observed the flow regimes, pressure drop, and heat transfer characteristics present in parallel square channels with a 1 mm hydraulic diameter where FC-72 was the working fluid. In addition to developing a new heat transfer coefficient model and pressure drop model, five flow regimes were categorized; annular-smooth, annular-wavy, transition, slug, and bubbly. Both annular-smooth and annular-wavy have a persistent core of vapor passing through the annulus formed by the condensate; however, in the wavy subtype there are distortions at the interface between the vapor and liquid phase. For the transitional flow regime, the distortions from the annular-wavy regime have grown such that the vapor is temporarily interrupted. In the slug regime, the vapor core is no longer persistent and instead presents as long vapor filled bubbles that still flow through the liquid annulus. The bubbly

flow regime is similar to the slug regime but differs in that the size of the bubbles has decreased such that their length is on the same order of magnitude as the channel diameter. While stratified flow can be observed in micro-channels under extreme circumstances, it is largely absent from micro-channels where the working fluid is undergoing phase change [40, 41].

Since during a phase change process the quality is constantly changing, a common way to study flow regimes is to use adiabatic flows where air and a liquid, such as water, are forced through a channel together at specific ratios to mimic the quality of a two-phase flow in a stable way [34]. Coleman and Garimella [42] observed the flow regimes present in four round tubes of diameters from 1.30 mm to 5.50 mm as well as a rectangular channel with a hydraulic diameter of 5.36 mm and an aspect ratio of 0.725. The smaller diameter suppressed the stratified flow regime causing the slug regime to occur for a larger portion of input ratios. Included in their work are flow-maps showing where each regime occurred on a graph of the liquid velocity versus the vapor velocity. In a similar study using vertically oriented triangular channels of hydraulic diameters from 0.866 mm to 2.886 mm, Zhao and Bi [43] found that the decreased diameter of the channels allowed for a new flow regime, capillary bubbly flow, to occur as well as greater occurrence of slug flow for the tested conditions. Ide et.al. [44] visualized and measured pressure drops in circular and rectangular channels with hydraulic diameters from 1.0 mm to 4.9 mm in both vertical and horizontal flow orientations. As the diameter decreased and capillary forces dominated, the flow regimes were more axisymmetric regardless of flow orientation; however, the flow regime which occurred for a given air-water input ratio was highly dependent on flow orientation. When flowing vertically, slug and annular flows became far more prevalent in the upward and downward flows respectively. Conversely in the horizontal flow, all the common flow regimes described by Kim et. al. [19, 20] were observed.

In the cases where condensation is occurring, the film thickness increases along the channel's length due to the vapor quality decreasing which affects the pressure drop, heat transfer, and flow regime [2, 12, 14, 15, 17, 18, 26, 27]. Wu and Cheng [45] investigated changing flow regimes in a 30-mm long trapezoidal micro-channel with a hydraulic diameter of 82.8 μm with steam as the working fluid for mass fluxes of 193 kg/m^{2}s to 475 kg/m^{2}s. As the annular film of condensate thickens, it reaches a location in the test section where the flow regime transitions to slug flow in a periodic manner described as injection flow. Wu and Cheng [45] also noted that in addition to the change in flow regime, the wall temperature at the transition location fluctuates at a frequency inversely correlated to mass flux. Ma et. al. [46] evaluated the axial changes in flow regime experienced by steam during condensation in micro-channels. Using trapezoidal channels with hydraulic diameters of 134.52 μm to 165.87 μm and steam mass fluxes from 90 kg/m^{2}s to 290 kg/m^2, they found that in addition to the expected dependence on mass flux and quality, there was also a strong dependence on the fluid properties such as surface tension. By comparing the location of the transition region using steam to that of a similar flow using R134a, they noted that the R134a would transition from annular to slug at much higher qualities for a given mass flux, and therefore much earlier in the flow condensation process. For example, at a mass flux of 200 kg/m^{2}s, the steam flow would transition at a quality of about 0.3 while the R134a would transition at a quality of about 0.5. As the mass flux increases, the quality required for transition lowered for both fluids, but more so for the steam.

While the thinner film due to forming an annulus or other non-stratified flow regime improves heat transfer rates, the decreased diameter available for the vapor phase to flow through increases the pressure drop required to maintain the flow rate [19-22]. This increased pressure drop required additional work from the closed-loop compressor or pump, which can negate the positive impact

on heat transfer. Therefore, enhancements to mini and micro-channels that increase the heat transfer coefficient without substantially increasing the pressure drop in condensers are of particular interest [3].

2.3 Filmwise condensation heat transfer

For a given channel shape and fluid, the three most significant variables affecting the condensation heat transfer are the hydraulic diameter, mass flux, and quality of working fluid; where decreasing the hydraulic diameter or increasing the mass flux or quality will increase the heat transfer coefficient [14, 17, 47, 48]. Sadaghiani [49] performed heat transfer experiments in circular channels of hydraulic diameters from 250 μm to 900 μm for steam mass fluxes of 20 kg/m^2s to 240 kg/m^2s. Sadaghiani [49] observed that while the heat transfer coefficient increases with decreased diameter for all cases, when the hydraulic diameter is less than 500 μm, that increase has a negative inflection (i.e., increasing the mass flux in these channels produces diminishing increases in the heat transfer coefficient). Despite this, decreasing the hydraulic diameter saw improvements in the heat transfer coefficient for all qualities and mass fluxes evaluated. At 50 kg/m^2s, the 250 μm channel had ~100% to ~250% increases in heat transfer coefficient for qualities of 0.2 and 0.75, respectively. For the mass flux of 200 kg/m^2s, the increase over the same diameter range was ~250% for all qualities in the same range.

While other variables such as the saturation pressure/temperature and the subcooling of the condensation surface can have an impact on the condensation process, the effects of these are significantly less than those experienced in boiling heat transfer [3, 50-54]. For condensation, raising the saturation pressure/temperature can increase the local heat transfer coefficient at the entrance of the channel. However, since raising the saturation pressure also lowers latent heat, the quality reduces more rapidly, causing the condensate film to increase in thickness and reduce the

overall heat transfer coefficient experienced by the channel [14, 17]. A numerical study by Adabi et. al [55] evaluating steam in an 18-mm circular tube predicts this heat transfer behavior where the heat transfer coefficient of the high pressure steam is high, but quickly decreases such that the net heat transfer coefficient in the channel is lower than that of steam at a lower pressure. Likewise, subcooling the condensing surface can increase the local heat transfer coefficient at the entrance of the channel while reducing the average heat transfer coefficient as shown by Zhang et. al. [56] with steam in ~17 mm twisted elliptical channels.

To predict the heat transfer coefficients for a mini-micro channel, a variety of correlations have been developed with limited application based on the fluid, flow properties, and channel geometry of the data used for the correlation development. Noting this, Kim and Mudawar [21, 22] developed a new approach to predicting the heat transfer coefficients using data from seventeen working fluids, hydraulic diameters from 0.424 mm to 6.22 mm, mass fluxes from 53 kg/m^{2}s to 1403 kg/m^{2}s, and qualities from 0 to 1. This correlation uses the modified Weber number to predict whether a flow while be annular (i.e., smooth-annular, wavy-annular, or transition regime) or slug/bubbly. The Lockhart and Martinelli parameter is used with newly developed constants, determined by the laminar or turbulent nature of the liquid and vapor phase of the two phase flow, as well as the annular or slug version of the correlation to predict the heat transfer coefficient with a MEA of 16.0% for the data set used in creating the correlation. While this correlation did consider a wide range of data in its development, the authors omitted some fluids (e.g., steam), surface enhanced channels, and non-circular/non-rectangular geometries from the data set. Because of this, the application of their correlation is still limited when using it to predict heat transfer coefficients with steam in modified or non-conventional mini/micro channels.

For channels that have non-conventional geometries (e.g., triangular, high aspect rectangular, or trapezoidal), the presence of corners allows for surface tension to draw the condensate away from the flat faces, reducing the thermal resistance there. As the quality of the working fluid decreases and the film thickness increases, the vapor-liquid boundary forms a progressively circular shape [31, 32, 57-59]. In a numerical study, Mghari et. al [31] determined that for steam minichannels with a hydraulic diameter of 250 μm, the larger ratio between the surface area and the cross-sectional area, the higher the heat transfer. Results for the Nusselt numbers in five channels with Reynolds numbers from 70 to 200 showed the worst performance in a square channel, while a rectangular channel with an aspect ratio of 4 had Nusselt numbers larger by about 55% to 70%.

2.4 Impacts of structures on filmwise condensation

Other approaches to enhance flow condensation heat transfer include physically modifying the condensing surface with structures designed to increase the condensing surface area, penetrate the film, or disrupt the film [2, 60, 61]. Royal and Bergles [62] evaluated steam condensing in seven circular channels with inner diameters of 11.5 mm to 13.8 mm, six of which had been modified with either a twisted tape or fin pattern inside the channel. For a mass flux range of 150 kg/m^{2}s to 583 kg/m^{2}s, the twisted tape increased the heat transfer coefficient over the smooth channel by 30% while the finned channels saw an enhancement up to 50% above that which would be expected from surface area increases.

Instead of using long interior fins that traverse the length of the condensing section, arrays of pin fins can also be used. Ho and Leong [60] used conical pin fins in a circular tube and compared them to dome shaped fins evaluated by Wang et. al. [61]. Using R134a in 8.7-mm channels, Ho and Leong [60] determined that helically arranged conical fins could enhance the heat transfer

coefficient by up to 2.44 times more than pressure drop was increased [63]. This increase in heat transfer coefficient enhancement relative to increased pressure was not found to be true of the dome fins used by Wang et al. [61]also using R134a in 8.7-mm channels. Aroonrat and Wongwises [64] utilized a 8.1-mm circular channel with R134a where dimples on the exterior of the tube were used to create hollow pin fins with depths of 0.5 mm, 0.75 mm, and 1 mm with diameters of 1 mm, 1.5 mm, and 2 mm, respectively, in the channel. While they were able to increase the heat transfer coefficient by up to 83%, the pressure drop was increased by up to 892% compared to a non-modified channel.

Similar to pin fins, a monolayer of particles can be affixed to a surface. Modak et. al [65] analyzed the effects of particle size of a hydrophobic monolayer of spherical particles on a gravity driven vertical plate condensing steam. Depending on the size of the particles, their effects on the heat transfer can be broken into three general categories: the roughness regime for particle diameters of 4 μm or less, the wick regime for particle diameters from 4 μm to 620 μm, and the fin regime for particle diameters greater than 620 μm. Both numerical and experimental results predict that up to a 25% increase in heat transfer could occur when the particle diameter is between 1 μm and 50 μm, with the greatest enhancement occurring at 10 μm.

2.5 Microgravity impacts on filmwise condensation

For microgravity applications, such as satellites or spacecraft, the impacts that gravity has on the condensation process need to be understood. Since performing experiments in micro-gravity settings is time and resource intensive, changing the orientation of test sections so that any gravitational impacts will work with or against the condensation process allows researchers to predict how the process would change in a micro-gravity setting [3, 4, 66, 67]. As the diameter of a channel decreases, the relative strength of surface tension and shear forces increase relative to

gravitational forces [4, 28]. Wen et al. [28] evaluated the annular distribution of R1234ze(E) in three mini/micro-channels and the associated heat transfer for flow condensation. For channel diameters less than 1 mm, gravitational effects were negligible where the mass fluxes tested ranged from 400-800 kg/m^{2}s [28]. However, for low mass velocity flows in particular, gravitational forces can still distort the shape of the annulus, preventing radial symmetry in horizontal channels [3, 28]. O'Neill et al. [68] studied FC-72 in 7.12-mm diameter channels where the condensing flow ran counter to, with, and horizontal to Earth's gravity with mass fluxes ranging from 50.3 – 360.3 kg/m^{2}s and concluded that mass velocity was the dominant factor in determining the heat transfer coefficient followed by quality and, for low flow rates, gravitational orientation.

In a numerical study of steam condensing in microgravity, Faghri and Chow [69] determined that as the steam condenses onto the cooling surface, the shear forces from the vapor flowing over it promotes a sucking or lift force that acts to remove the condensation from the surface. Performing experiments for microgravity conditions is challenging due to the limited available and high cost associated with the available platforms, such as parabolic flights or the ISS [3, 4]. Due to this no, experimental papers were located for steam condensation in micro-gravity conditions.

2.6 Dropwise condensation

Unlike in filmwise condensation, where the entire surface is coated in the condensate film, dropwise condensation occurs when the nucleating droplets are removed from the surface quickly, allowing more droplets to form in direct contact with the cooling surface. Dropwise condensation can be achieved by modifying a surface to be hydrophobic via either coating the surface with a hydrophobic compound or by adding nanostructures to induce a Cassie or partial wetting state [12, 16]. When dropwise condensation occurs, it can result in heat transfer enhancements up to 10×;

however, both coatings and nanostructures face durability challenges preventing widespread adaptation. [9, 70-73].

Chen and Derby [9] studied a 0.952-mm-diameter mini-channel to compare the heat transfer performance of steam when either dropwise or filmwise condensation were occurring by coating their test section in a hydrophobic compound, Teflon AF. The hydrophobic coating increased the heat transfer coefficient by 480%-614% for mass fluxes of 50 kg/m^{2}s, 75 kg/m^{2}s, and 100 kg/m^{2}s. Chen et al. [9, 48] also determined the droplet departure diameter and sweeping period varied inversely with the mass flux and steam quality allowing for higher heat transfer coefficients at higher mass fluxes and qualities.

Alizadeh-Birjandi et al. [8] created a biphilic patten, where hydrophilic and hydrophobic surfaces were created in a checkered pattern on a vertical plate and cooled, to produce condensation from moist air. While Alizadeh-Birjandi et al. [8] did not collect heat transfer date, they observed an increase in the droplet formation growth and departure on their biphilic surface as compared to either a purely hydrophilic or hydrophobic surface. Orejon et al. [11] studied a microstructured surface to induce both filmwise and dropwise condensation at the same time. Silicon micropillars with a diameter of 50 μm were spaced at either 10 μm, 25 μm, or 50 μm intervals on a cooling surface tilted at 30° and condensing water from moist air. Orejon et al. [11] found that without using a hydrophobic surface, dropwise and filmwise condensation would occur concurrently so long as the micro-pillars were 25 μm. Based on the data they collected, Orejon et al. [11] created a model that predicts heat transfer coefficients between that of a purely hydrophilic or hydrophilic surface.

2.7 Research objectives

Recent literature reviews within the field of flow condensation have consistently noted that there is a general need for more experimental work to be done for a variety of channels with unique geometries, orientations, flow conditions, surface wettabilities, and fluids [2, 12, 14, 15, 17]. In particular, research on modified surfaces utilizing steam as the working fluid is lacking, which is important due to the significant difference in surface tension it has when compared to refrigerants. As such, the objectives of this study are to utilize an open-loop steam apparatus using temperature, pressure, and mass flow rate measurements as well as high-speed videography to:

- Investigate the impacts of hemispherical structures on the condensing surface on heat transfer coefficients, film disruption, and pressure drops.

- Determine the impacts of porous monolayers and hemispheres on the condensing surface on heat transfer coefficients, film disruption, and pressure drops.

- Understand the effects of gravitational orientation on condensation heat transfer coefficients, film behavior, and pressure drops.

- Determine the impacts of hydrophobicity on condensation heat transfer coefficients, film, and pressure drops as well as orientation (i.e., gravitational effects).

Chapter - 3 Flow condensation experimental apparatus

This chapter discusses the experimental apparatus and test coupons as well as the data collection procedures and uncertainty analysis. A single-phase validation of the experimental apparatus is also included.

3.1 Experimental apparatus

Experiments were conducted using an open-loop steam apparatus, shown in Figure 3.1, designed to measure condensation heat transfer coefficients, pressure drops, and allow for visualization of the condensation process. Steam was regulated to 250 kPa for all experimental conditions and passed through a separator to remove any water and a filter system to remove any contaminates which may be in the steam supply. Due to uncertainty regarding the initial steam quality, the steam was superheated by 20°C to 30°C above saturation temperature. The superheated steam then passed through a pre-condenser to control the quality of the steam entering the test section. The cooling water was supplied by a constant-temperature bath (Neslab RTE-221), and its mass flow rate was measured via a Coriolis flow meter (CMFS015M, Micro Motion), and its temperature was measured by two T-type thermocouples (Omega; T-Q-SS-116-G-3).

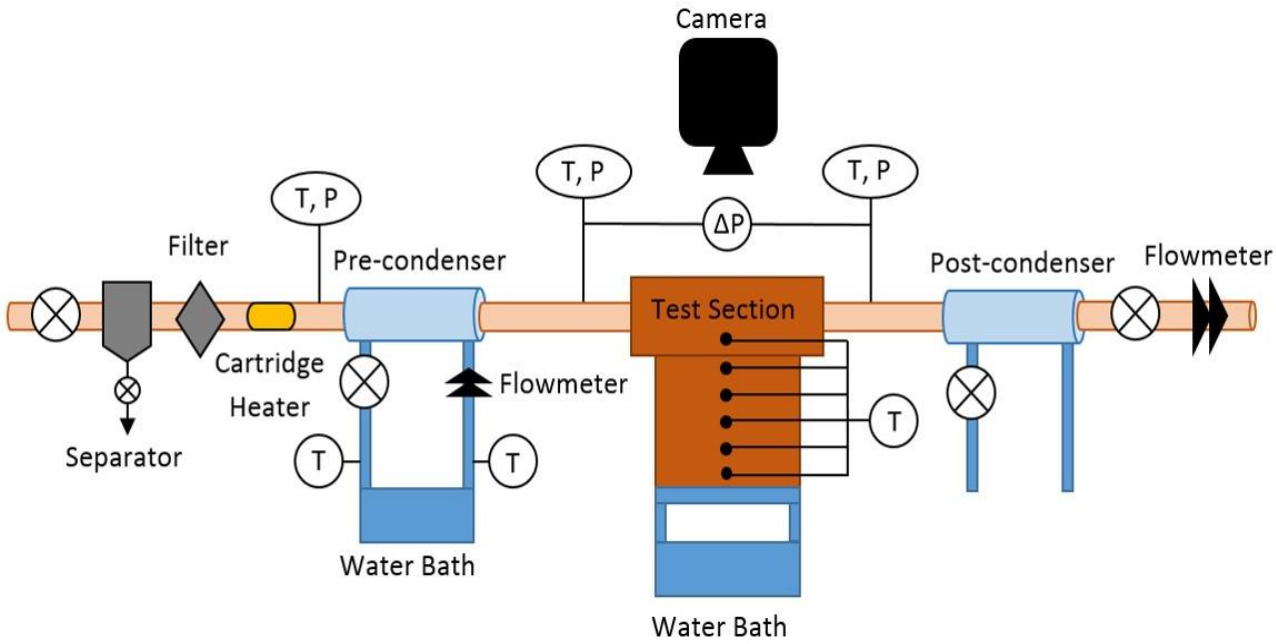

Figure 3.1 Open-loop experimental apparatus for steam condensation heat transfer and simultaneous flow visualization [1]

The steam temperature was measured before and after the pre-condenser using T-type thermocouples (Omega; T-Q-SS-116-G-3) and as well as after passing through the test section. A differential pressure transducer (Omega; PX409) was used to measure the pressure drop across the test section. Five T-type thermocouples (Omega; TJC36-CPSS-062U-2) installed in the cooling block were used to calculate the heat flux leaving the steam and entering the cooling water supplied by a second constant-temperature bath. A sixth T-type thermocouple installed in the test coupon was used to determine the wall temperature in the channel. To determine the effects of gravity on flow condensation, the same apparatus was used where the test section was inverted such that the cooling surface was above the steam flow as seen in Figure 3.2. In both orientations, visualization of the film was conducted using Leica Z16 APO macroscope and a FASTEC IL3 high-speed camera set to collect 500 frames-per-second at 2X magnification and illuminated by a Leica LED 5000 SLI Spotlight Illuminator. Temperature and pressure data were collected using LabVIEW and a cDAQ-9174 with NI TB-9214 and NI 9207.

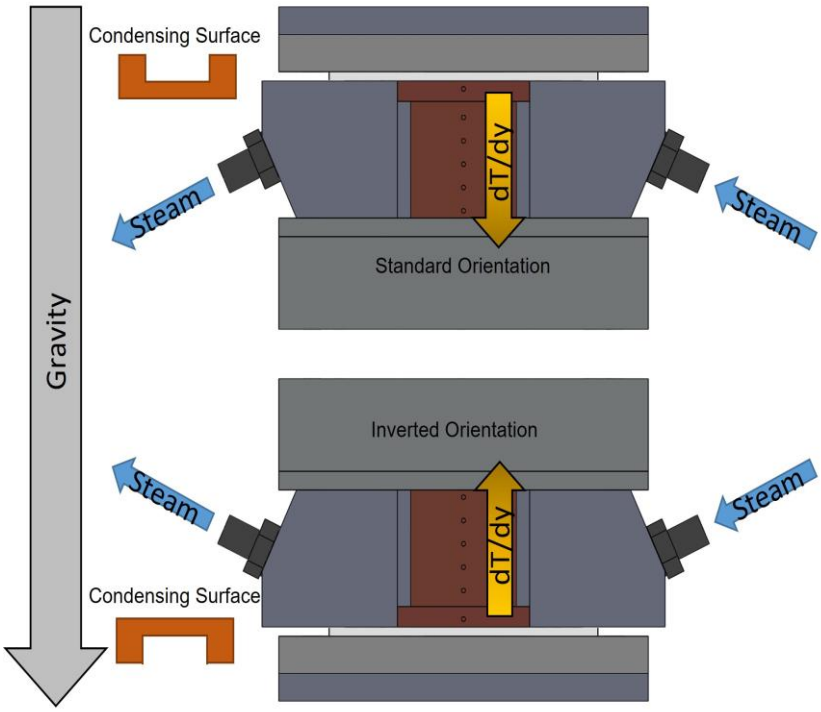

Figure 3.2 Test section, including coupons and heat flux block where (above) the test section is in the standard orientation or (below) the test section is in the inverted orientation [1]

3.2 Test coupons

Two types of test coupons, shown in Figure 3.3, were constructed out of oxygen-free copper and with a channel whose hydraulic diameter was 1.9 mm. The first type of coupon had a channel with a flat rectangular cross section. The second test section had copper hemispheres, whose hydraulic diameter was calculated by using the length averaged cross sectional area and perimeter. Three coupons using the rectangular cross section were constructed. In one, no additional structures were added and is referred to as the plain coupon. The other two of these coupons had a monolayer of copper microparticles sintered onto the channel surfaces, which are referred to as the 100 µm monolayer coupon and the 200 µm monolayer coupon. Two mound coupons were constructed with 16, 2-mm diameter hemispheres. In the first of these, the solid mound coupon, a solid copper ball bearing was sintered into hemispherical grooves machined into the copper

coupon. The other mound coupon used 200 µm particles sintered together to form the hemisphere and is referred to as the 200 µm mound coupon.

Table 3.1 Coupon channel dimensions

	length (mm)	width (mm)	depth (mm)	surface area (mm^2)
Plain	40	5	1.2	363.2
100 µm monolayer	40	5	1.35	-
200 µm monolayer	40	5	1.28	-
Solid mound	40	5	1.5	413.5
200 µm mound	40	5	1.5	-

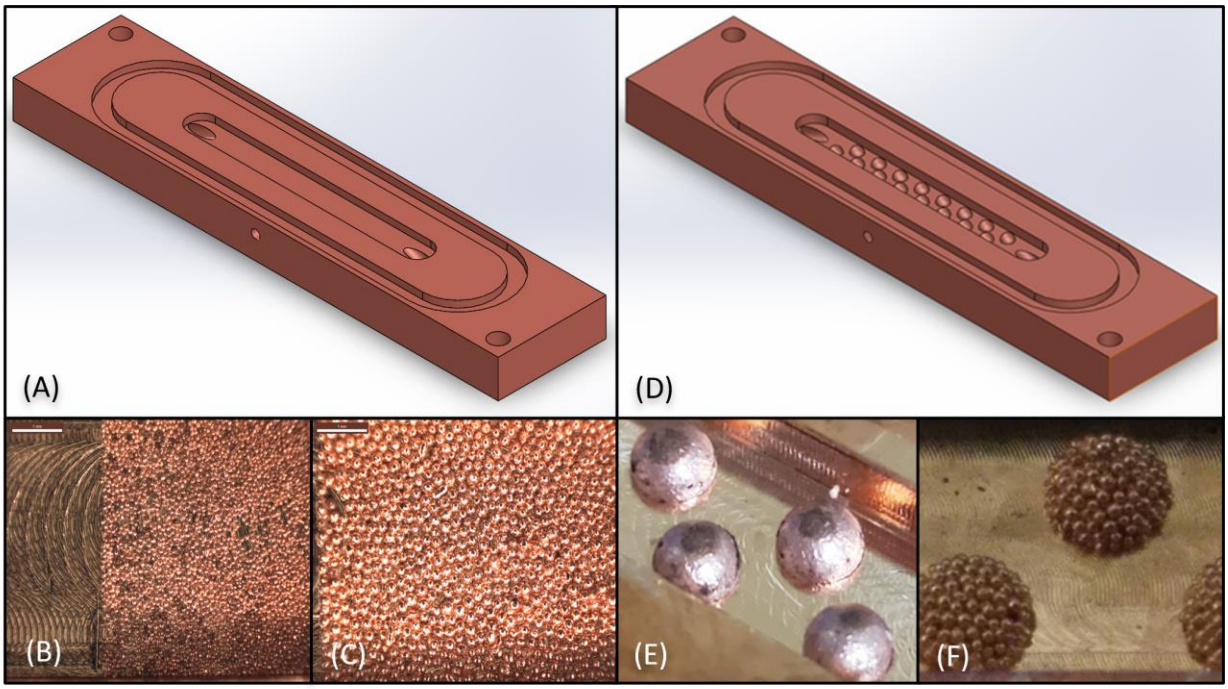

Figure 3.3 Coupons with 1.9-mm hydraulic diameter; (a) plain coupon with no additional structures, (b) 100-µm particle monolayer, (c) 200-µm particle monolayer, (d) mound coupon with 2-mm diameter hemispheres, (e) solid mound, (f) 200-µm particle mounds

The sintering process for the 100 µm monolayer, 200 µm monolayer, solid mound, and 200 µm mound coupons was conducted by collaborators Drs. Hwang and Egbo at Wichita State University; a description of the sintering process follows. The copper coupon surfaces were cleaned using acetone, and then dried under ambient conditions. Two types of stainless-steel molds were fabricated: one to hold a single layer of sintered particles for the monolayer coupons and a

mold with hemispherical indents for the solid mound and 200 μm mound coupons. The molds were designed and fabricated at KSU. For the sintering process, molds were lightly secured to the copper surfaces, and were coated with carbon powder to prevent the mold from adhering to the copper particles. For the solid mound coupon, sixteen 2-mm copper balls were placed in hemi-spherical grooves machined into the bottom of the coupon's channel. Coupons were sintered in a tube furnace (OTF-1200X); the temperature profile of the furnace during the sintering process is shown in Figure 3.4; the peak temperature used in this study was 1273 K. Following the sintering process, the molds were removed from the copper coupons.

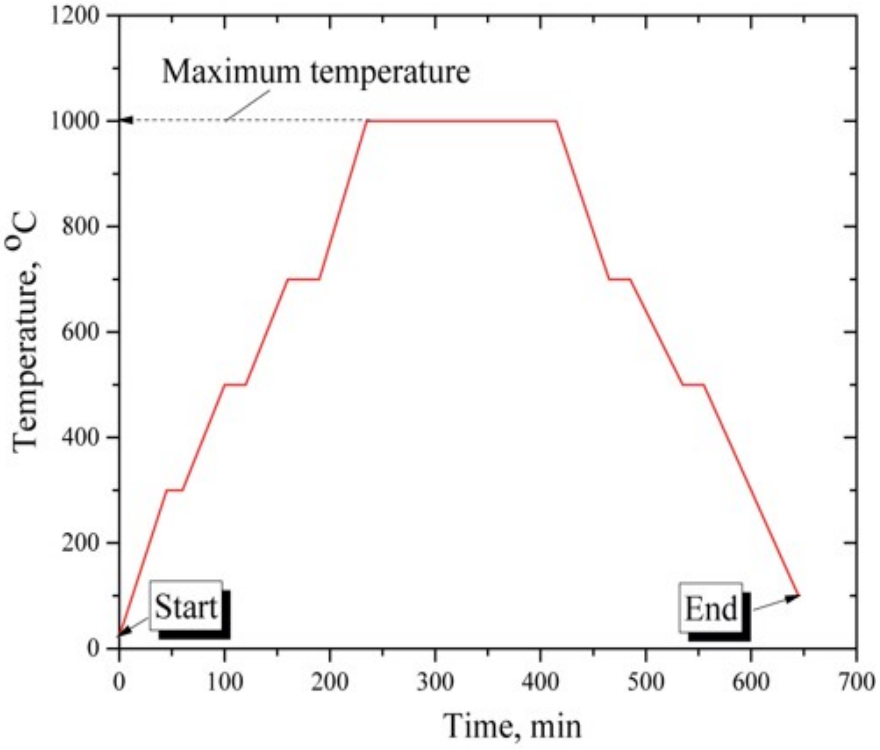

Figure 3.4 Sintering temperature as a function of time with the peak temperature shown [1]

3.3 Data reduction

Fourier's Law was utilized to determine the heat transfer rate, which is necessary to calculate heat transfer coefficients, *h*,

$$\dot{Q}_{block} = -kA_{block}\frac{dT}{dy}_{block} \quad \textbf{3.1}$$

$$h = \frac{\dot{Q}_{block}}{A_{surf}(T_{steam} - T_{wall})} \quad \textbf{3.2}$$

where the temperature gradient in the cooling block, *dT/dy*, was calculated using the least squares method; A_{surf}, was the surface area where condensation occurs; A_{block} was the cross-sectional area of the cooling block; and *k* was the thermal conductivity of the oxygen-free copper. For the mound coupon, the planform area of 363 mm^2 was typically used instead of the actual area of 416 mm^2. Fluid temperature, T_{steam}, was determined using the saturation temperature associated with the pressure of the two-phase steam in the coupon, assuming a linear pressure drop. The wall temperature, T_{wall}, was measured using a thermocouple in the coupon 1.5-mm below the bottom of the mini-channel.

3.4 Experimental uncertainties

All measurement devices were carefully calibrated. The T-type thermocouples were calibrated in a water bath at 5°C increments from 5°C to 60°C, as well as in boiling water and in an ice bath, and compared against a reference thermometer, resulting in a thermocouple uncertainty of ± 0.2 °C. For the temperature gradient from the test section, the uncertainty was calculated using the following equation [74],

$$\omega_{\frac{dT}{dy}} = \sqrt{\omega_T^2 + \left(\frac{q'' D_{hole}}{6k}\right)} \sqrt{\frac{1}{\sum_{i=1}^{N}(y_i - \bar{y})^2}} \quad \textbf{3.3}$$

where D_{hole}, 0.0625 in, is the diameter of the thermocouple hole, q'' is the heat flux, y is the position of each hole along the direction of the thermal gradient, $\bar{y}$ is the average thermocouple position, and ω represents the uncertainty. With the high thermal conductivity of the oxygen-free copper, and the relatively small size of the thermocouple holes compared to the distance between them, the gradient uncertainty was less than ± 10°C/m for all filmwise condensation cases and was the largest contributor of uncertainty for the heat transfer through the cooling block, and by extension, for the heat transfer coefficient. In the dropwise cases, the largest source of uncertainty came from the small temperature difference between the steam temperature and the surface temperature.

Pressure transducers were calibrated using a deadweight tester, which allowed for a 0.25% full scale error which corresponded to an uncertainty of ±1.7 kPa. Since the pressure and temperature of a two-phase fluid are not independent, the pressures from the inlet and outlet of the test section were averaged and used to determine the temperature of the steam, T_{steam}, in the test section with an uncertainty of ± 0.5°C. Subsequently, the uncertainties for heat transfer coefficients were calculated,

$$\omega_h = \quad \textbf{3.4}$$

$$\sqrt{\left(\frac{\partial h}{\partial \dot{Q}_{block}} \omega_{\dot{Q}_{block}}\right)^2 + \left(\frac{\partial h}{\partial A_{surf}} \omega_{A_{surf}}\right)^2 + \left(\frac{\partial h}{\partial T_{steam}} \omega_{T_{steam}}\right)^2 + \left(\frac{\partial h}{\partial T_{surf}} \omega_{T_{surf}}\right)^2}$$

where the uncertainties were dependent on uncertainties in the block heat transfer rate, $\dot{Q}_{block}$, surface area, A_{surf}, two-phase saturation temperature of the condensing steam, T_{steam}, and surface temperature, T_{surf}.

3.5 Single-phase validation

To validate the experimental apparatus and test section heat transfer measurements, single-phase validation experiments were conducted. Steam was cooled to subcooled water at 250 kPa and 50 °C to 70°C for a single-phase validation using the plain coupon. This validation used two metrics; the first was to compare the amount of energy which was exiting the water, $\dot{Q}_{water}$, to that which was passing through the cooling block, $\dot{Q}_{block}$, from equation 1,

$$\dot{Q}_{water} = \dot{m} c_p (T_{in} - T_{out}) \quad \textbf{3.5}$$

where $\dot{m}$ is the mass flow rate of the fully condensed water, $c_p$is the specific heat at constant pressure, and T_{in} and T_{out} are the temperature entering and exiting the test section respectively.

The second validation compared measured single-phase Nusselt numbers to the correlation created by Muzychka and Yovanovich [75] for non-circular ducts, which provides an upper and lower bound for the single-phase Nusselt number,

$$u = \left[\left(c_4 \frac{f(Pr)}{z^*} \right)^m + \left(\left(c_2 c_3 \left(\frac{f(Re)}{z^*} \right) \right)^{\frac{5}{3}} + \left(c_1 \frac{f(Re)}{8\pi^{0.5} \varepsilon^{\gamma}} \right)^5 \right)^{\frac{m}{5}} \right]^{\frac{1}{m}} \quad \textbf{3.6}$$

$$f(Re) = \left[\left(\frac{12}{\varepsilon^{1/2}(1+\varepsilon)\left(1 - 192\left(\frac{\varepsilon}{\pi^5}\right) tanh\left(\frac{\pi}{2\varepsilon}\right)\right)} \right)^2 + \left(\frac{3.44}{z^{+1/2}} \right)^2 \right]^{1/2} \quad \textbf{3.7}$$

$$f(Pr) = \frac{0.564}{(1 + (1.909 Pr^{1/6})^{9/2})^{2/9}} \quad \textbf{3.8}$$

where the values of c_1, c_2, c_3, c_4, and *f(Pr)* are determined by the boundary conditions, ε is the aspect ratio of the channel, and γ is the shape parameter which is 1/10 for the upper bound and -3/10 for the lower bound. Additionally, *f(Pr)*, *f(Re)*, and *Nu* are the functions for the Prandtl number, Reynolds number, and Nusselt number, respectively. The heat transfer from the subcooled

water to the cooling block was within 20% for all experimental points. For single-phase heat transfer, uncertainty is generally higher than for two-phase heat transfer due to the temperature in single-phase flows changing as thermal energy is removed. If the temperature difference between the inlet and outlet is too large, the assumption that the heat transfer through the coupon and cooling block is one-dimensional also breaks down causing further difference between the heat transfer rates in the energy balance. However, all Nusselt numbers were within or within the error of the predicted value range, as shown in Figure 3.5. The single-phase energy balance and Nusselt number analysis confirmed that the apparatus operated as predicted and that two-phase heat transfer measurements have acceptable accuracy.

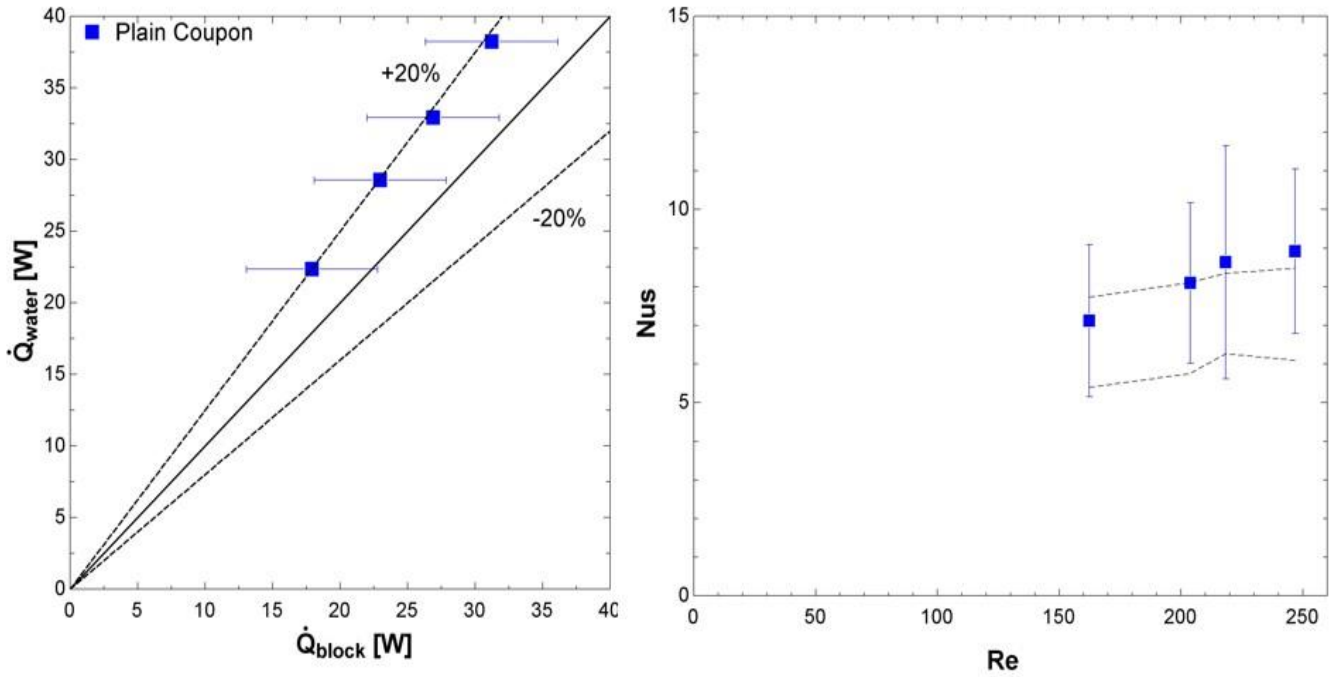

Figure 3.5 Single phase validation, including (left) energy balance and (right) measured Nusselt numbers compared to predictions by the single-phase Muzychka [75] correlation figure from [1]

3.6 Two-phase experimental procedure

Two-phase data were collected using the following procedure. For a given test coupon, the steam mass flow rate was adjusted to the mass flux for which the data were being taken. Once the mass flux was stabilized and the steam was superheated, the steam quality was adjusted using the pre-condenser. Once the desired mass flux, steam quality, and steady-state conditions were reached, data from the pressure transduces, thermocouples, and the flowmeter would be recorded for 120 s. If needed, adjustments would be made before repeating the data recording process. After 15 minutes, the data for the same quality and mass flux would be recorded again to ensure that the system was operating under steady-state conditions. Once confident that the steam properties were within tolerances, and the data were collected, the insulation covering the top of the test section would be removed for flow visualization. The camera and lights were moved into place and high-speed video at 500 fps were recorded. At this time, the insulation was placed back on the test section and the pre-condenser would be adjusted for the next data point.

Chapter - 4 Filmwise condensation in the standard orientation

Heat transfer coefficients, condensate film, and pressure drop results are discussed in this chapter where all coupons are hydrophilic and in standard orientation (i.e., experiencing lower surface condensation, where gravity pulls the film towards the condensing surface).

4.1 Plain coupon

4.1.1 Condensation heat transfer coefficients

Condensation data collected from the plain coupon, in the standard orientation (i.e., condensation on lower surface), served as a baseline to compare against for any enhancement. For a mass flux of 50 kg/m^{2}s and qualities from 0.20 to 0.87, the flow condensation heat transfer coefficients range from 22,200 W/m^{2}K to 53,000 W/m^{2}K. At the higher mass flux of 125 kg/m^{2}s and qualities from 0.33 to 0.97, the flow condensation heat transfer coefficients ranged from 40,800 W/m^{2}K to 95,200 W/m^{2}K. For both mass fluxes, the heat transfer coefficients increased nearly linearly with quality; similarly, the heat transfer coefficients increased with the increasing mass flux. To compare the other coupons, a third-degree polynomial was curve fit to these measured heat transfer coefficients so that an enhancement ratio could be calculated for any quality. The R^2 values for these polynomial curve fits were 0.9908 and 0.9986 for the 50 kg/m^{2}s and 125 kg/m^{2}s data sets, respectively. Heat transfer coefficients for all the plain coupon at both mass fluxes is shown in Figure 4.1.

Table 4.1 Plain coupon curve fit coefficients and R^2 values

$h_{curve\ fit} = A+Bx+Cx^2+Dx^3$					
Mass flux (kg/m^{2}s)	A	B	C	D	R^2
50	3764.78	111410	115240	58844.2	0.9908
125	4123.34	167001	219598	147720	0.9986

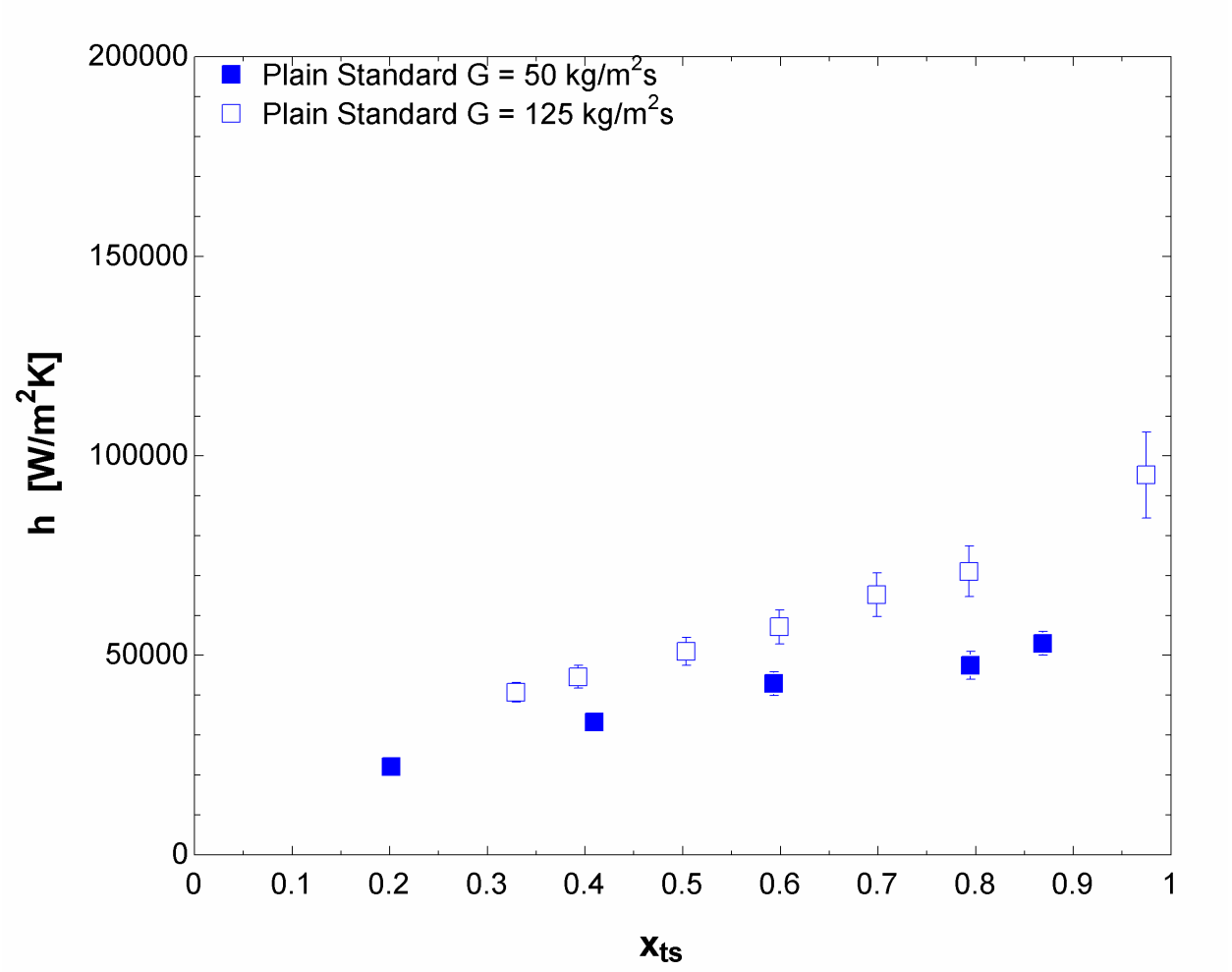

Figure 4.1 Heat transfer coefficients for the plain coupon standard orientation

4.1.2 Kim and Mudawar [21] correlation for mini-channel condensation

The condensation heat transfer coefficients for the plain coupon in the standard configuration were compared to the values predicted by the Kim and Mudawar [21] correlation for condensing in mini/micro channels. The Mean Absolute Percentage Error (*MAPE*) for a mass flux of 50 kg/m^{2}s was 38% and for a mass flux of 125 kg/m^{2}s was 16%, as shown in Figure 4.2,

$$MAPE = \frac{1}{n}\sum_{i=1}^{n}\left|\frac{h_{pred} - h_{exp}}{h_{exp}}\right| \qquad \textbf{4.1}$$

where h_{pred} is the heat transfer coefficient predicted by the correlation, and h_{exp} is the observed heat transfer coefficient from the experimental apparatus. Since the flow regimes influence the predicted heat transfer coefficients, it should be noted that for the mass flux of 50 kg/m^{2}s, the flow regimes predicted by the Kim and Mudawar [21] correlation were all either in the transitional or slug regimes, while for the mass flux of 125 kg/m^{2}s, the predicted flow regimes were either wavy-annular or transitional.

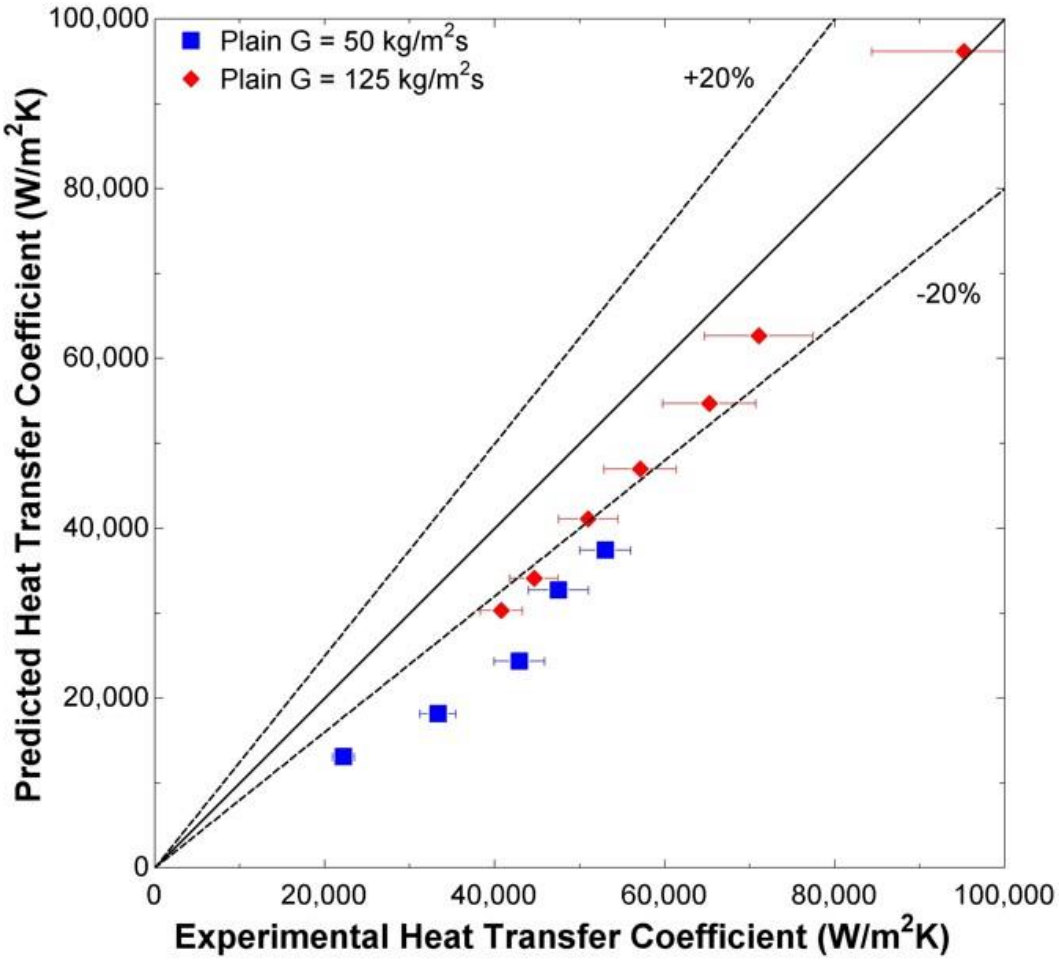

Figure 4.2 Flow condensation heat transfer coefficients predicted by the Kim and Mudawar [21] model for the plain coupon in standard orientation figure from [1]

4.1.3 Film visualization during condensation in the plain coupon

By using a high-speed camera, the flow condensation was observed at 500 frames per second. In the plain coupon, condensate film flow was generally smooth for both mass fluxes observed. At the lower mass flux and low qualities, the film had almost no disturbances apart from the occasional "wave" across the entire mini-channel, which can been seen in Figure 4.3 (A) where the disturbance is wide and smooth. In Figure 4.3 (B) and (C) where the qualities are 0.6 and 0.8, the increased shear forces increase the frequency of waves and increase their roughness. For a mass flux of 125 kg/m^{2}s, when the quality is low, x = 0.3 as shown in Figure 4.3 (D), the flow is similar to what was seen with a mass flux of 50 kg/m^{2}s but with a less smooth interface. As the quality increases, shown in Figure 4.3 (E) and (F) the flow does not have consistent "waves", but instead a portion of the condensation is swept up into the vapor flow causing a hazy appearance.

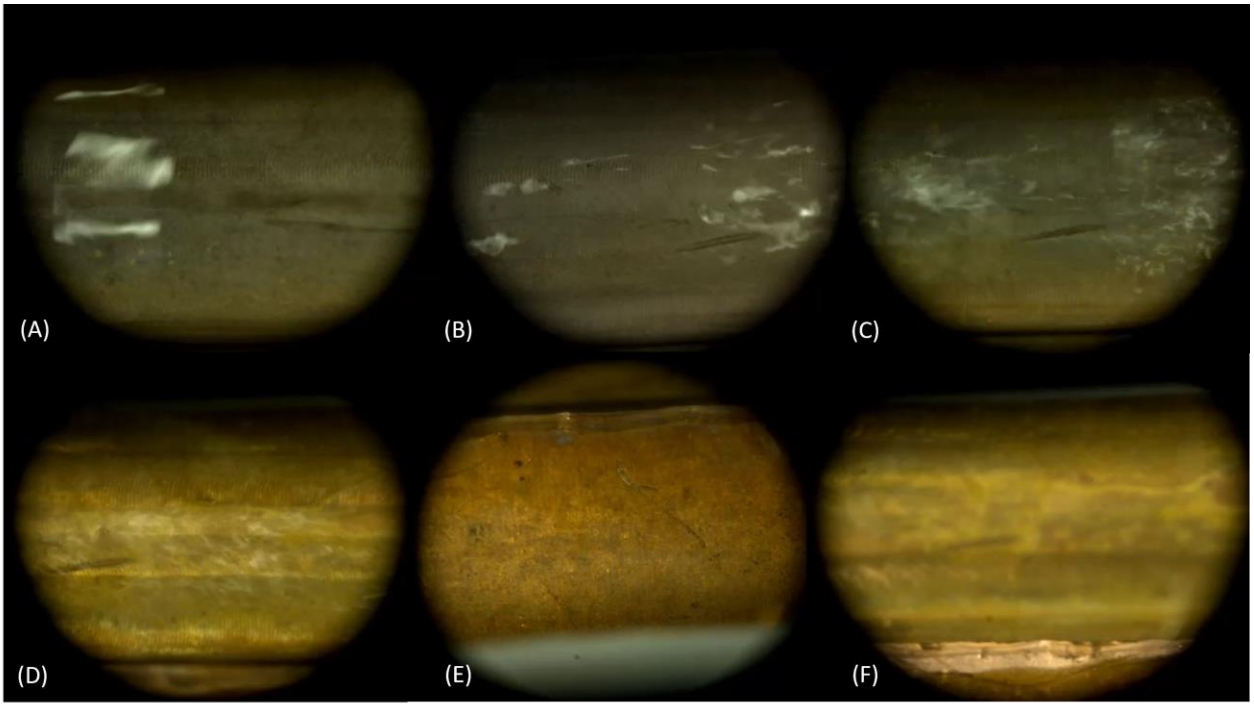

Figure 4.3 Films in plain coupon in standard orientation at: (A) a mass flux of 50 kg/m^{2}s and quality of 0.2, (B) a mass flux of 50 kg/m^{2}s and quality of 0.6, (C) a mass flux of 50 kg/m^{2}s and quality of 0.8, (D) a mass flux of 125 kg/m^{2}s and quality of 0.3, (E) a mass flux of 125 kg/m^{2}s and quality of 0.6, (F) a mass flux of 125 kg/m^{2}s and quality of 0.8

4.2 Solid mound coupon

4.2.1 Condensation heat transfer coefficients

For the mound coupon, condensation heat transfer coefficients were calculated using its planform area, though the actual surface area of the mound coupon is 13.8% larger than that of the plain coupon. In Figure 4.4 the heat transfer coefficient of the solid mound and plain coupons are shown where the actual surface area (i.e., including the mound surface area) was used. This is the only place where heat transfer coefficients are not reported using the planform area. In Figure 4.5 the heat transfer coefficients of the two coupons under the same conditions is shown using the planform area. With a mass flux of 50 kg/m^{2}K and qualities from 0.21 to 0.81, the heat transfer coefficients ranged from 33,100 W/m^{2}K to 56,200 W/m^{2}K. This corresponds to a linearly decreasing enhancement of 47% at a quality of 0.21, to a 13% enhancement at a quality of 0.81. At a mass flux of 125 kg/m^{2}s, the heat transfer coefficients range from 44,300 W/m^{2}K to 132,000W/m^{2}K at qualities of 0.20 to 0.81, respectively. The enhancement has a generally parabolic shape as a function of quality where the greatest enhancement occurring at the low and high quality points. At a quality of 0.20, the heat transfer coefficient is enhanced 48%, and at a quality of 0.81, it is enhanced by 79%. The lowest enhancement occurs at a quality of 0.5 and corresponds to an enhancement of 20%. This parabolic enhancement trend is best explained by the relative size of the mounds to the film as well as the disruption of film flow which occurred due to them, as discussed in the subsequent section. These heat transfer enhancements are similar to those found by Aroonrat and Wongwises [64], using R134s, with hollow pin fins and a maximum increase of 83%, though this enhancement is lower than the 244% enhancement measure by Ho et al. [63] using R134a with conical fins lining the interior of the channel. Ho and Leong [76]

investigated condensing steam on vertical plates with an array of conical films, which resulted in an increase of 146%, however this differs from the present study as Ho and Leong studied gravity-driven film condensation.

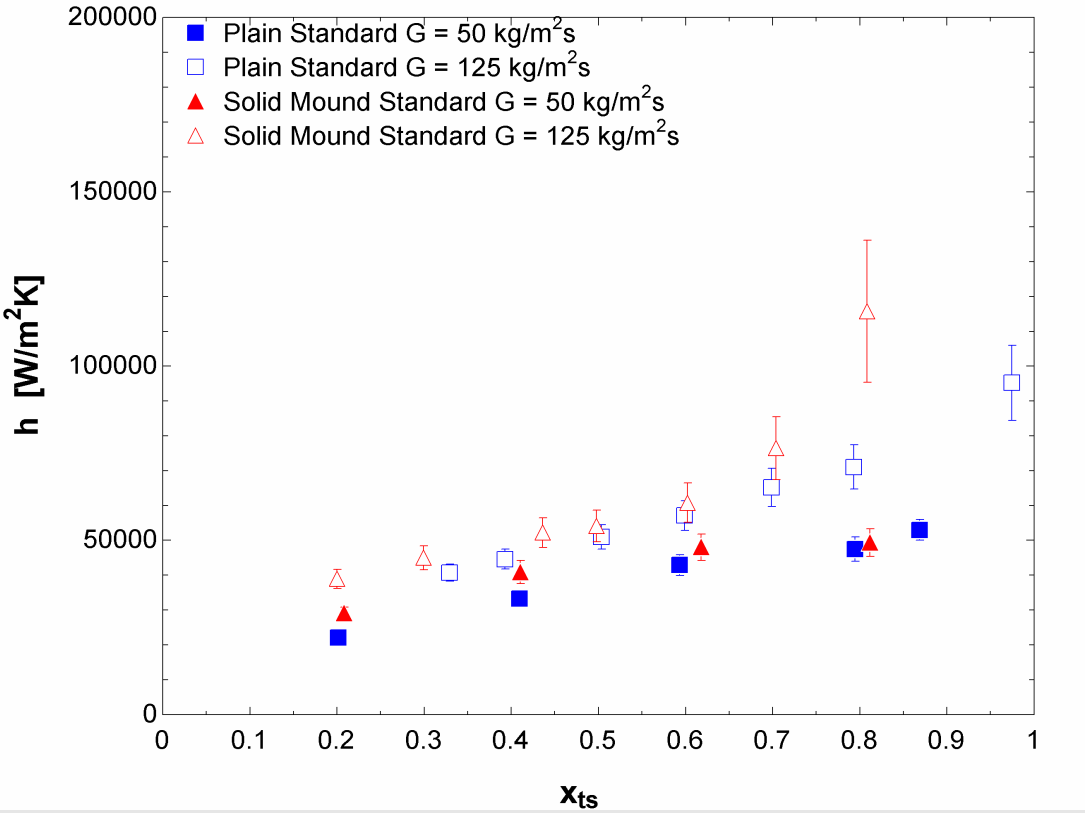

Figure 4.4 Heat transfer coefficients of the solid mound and plain coupon using the total surface area

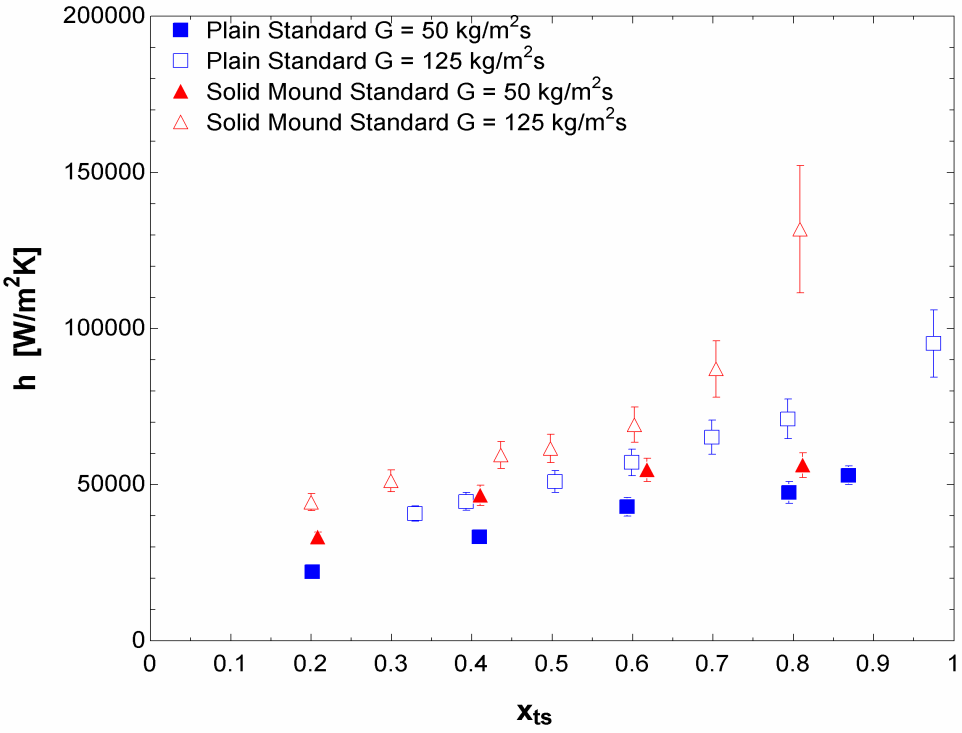

Figure 4.5 Heat transfer coefficients of solid mound coupon and plain coupon in standard orientation

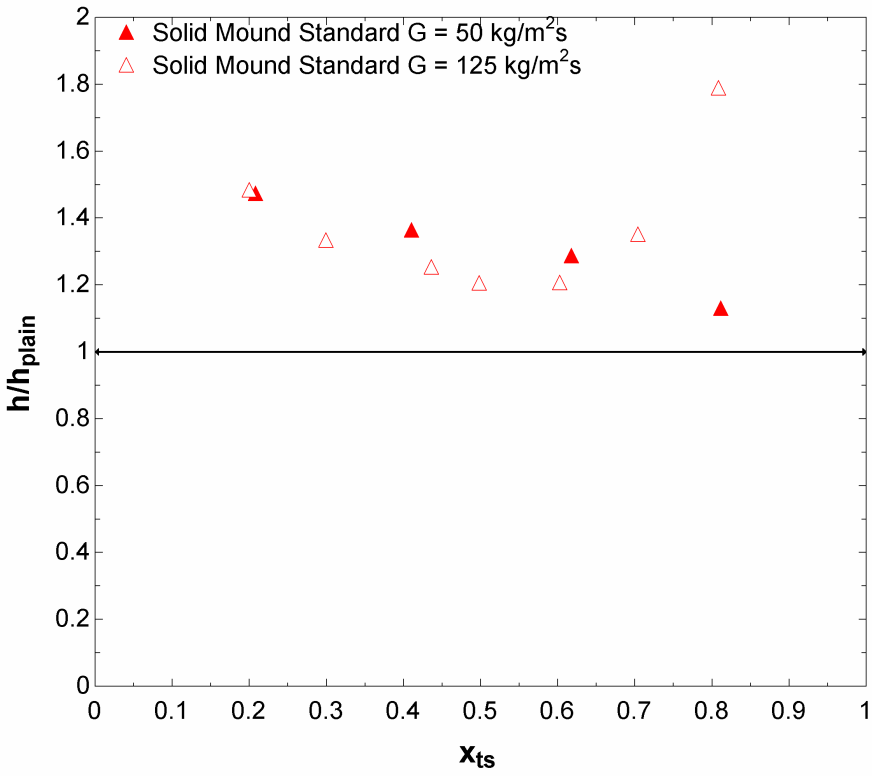

Figure 4.6 Heat transfer coefficient enhancement in the solid mound coupon compared to the plain coupon in standard orientation

4.2.2 Film visualization and thickness in the mound coupon

For the mound test section, the mounds themselves served to disrupt the flow by preventing the film from flowing in a straight line down the test section as compared to the plain coupon where the flow was unobstructed. Figure 4.7 shows the condensed film in both channels at a quality of 0.6 for both mass flow rates. For the flow in the solid mound coupon at a mass flux of 50 kg/m^{2}s and a quality of 0.6, Figure 4.7C, the mounds create a wake in the film and force it to either flow over or around the mounds, thinning the film above the mounds while also increasing the film velocity above the substrate. For the solid mounds with higher mass flux, Figure 4.7D, a large portion of the liquid phase is suspended in the vapor phase, resulting in a thin film at all points on the surface. In Figure 4.8, both the wake effects from the mounds as well as the winding of path that the flow is forced to take around the mounds can be seen 4 milliseconds.

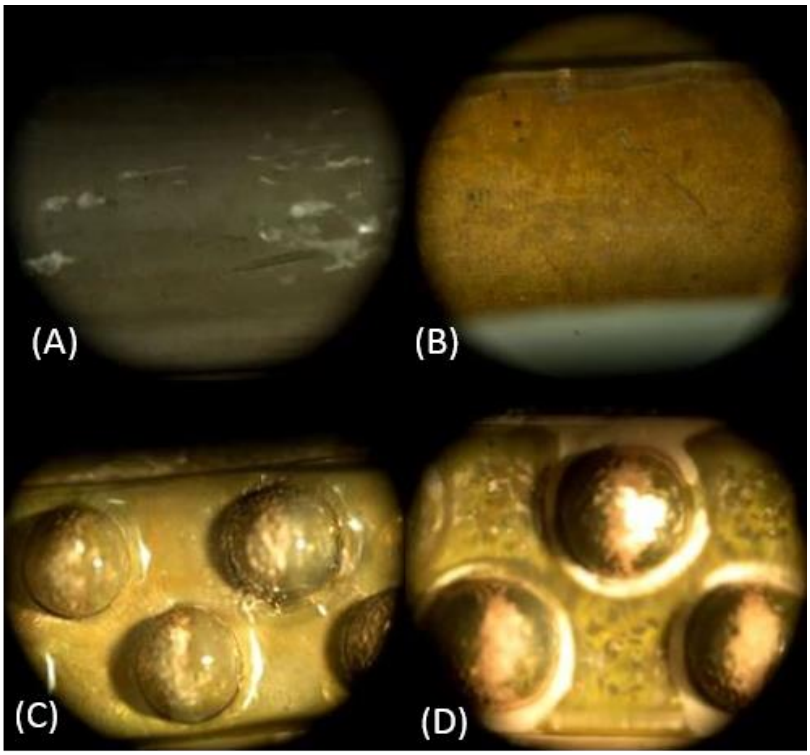

Figure 4.7 Condensed film in standard orientation plain and solid mound coupons with a quality of 0.6; (A) plain coupon with a mass flux of 50 kg/m^{2}s, (B) plain coupon with a mass flux of 125 kg/m^{2}s, (C) mound coupon with a mass flux of 50 kg/m^{2}s, (D) mound coupon with a mass flux of 125 kg/m^{2}s figure from [1]

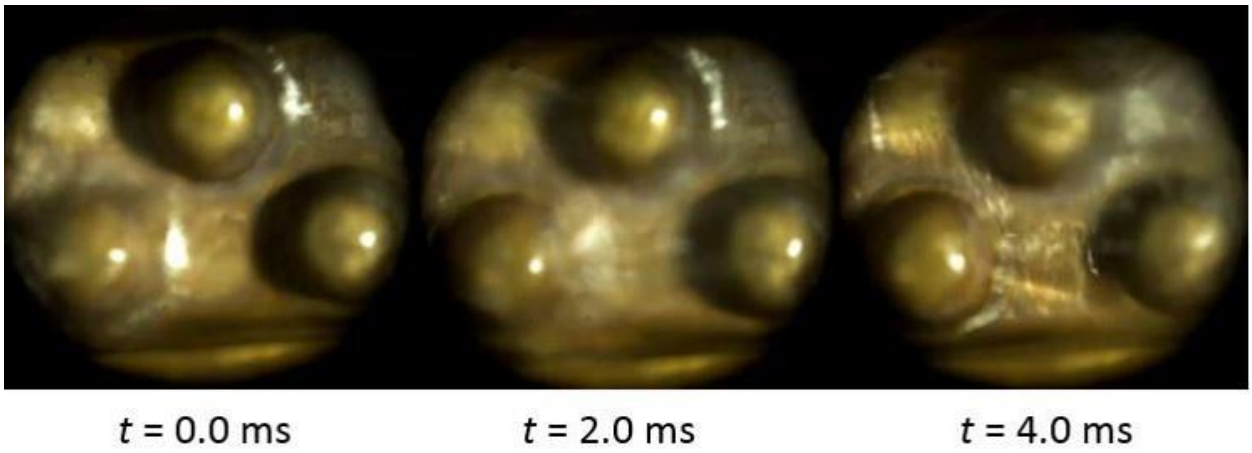

Figure 4.8 Mound disruption on film at (Left) *t* = 0 ms, (Middle) *t* = 2.0 ms and (Right) *t* = 4.0 ms at a mass flux of 50 kg/m^{2}s and a quality of 0.2 figure from [1]

To show the significance of the mounds, a maximum film depth was calculated using the Butterworth [77] correlation to estimate the volume of condensed water in the film. Figure 4.9 shows the maximum depth that the film could reach (i.e., estimated film thickness),

$$d_{film} = (1 - \alpha) d_{channel} \tag{4.2}$$

$$\alpha = \frac{1}{1 + 0.28 X_{vv}^{0.71}} \tag{4.3}$$

$$X_{vv}^2 = \left(\frac{1 - x}{x}\right) \frac{\rho_g}{\rho_l} \frac{\mu_l}{\mu_g} \tag{4.4}$$

where d_{film} is the maximum possible film depth, $d_{channel}$ is the depth of the channel, α is the volumetric fraction of vapor in the channel, X_{vv} is the Martinelli parameter for viscous-viscous flows, x is the steam quality, ρ and μ are the density and viscosity of the liquid, l, and vapor, g, phases.

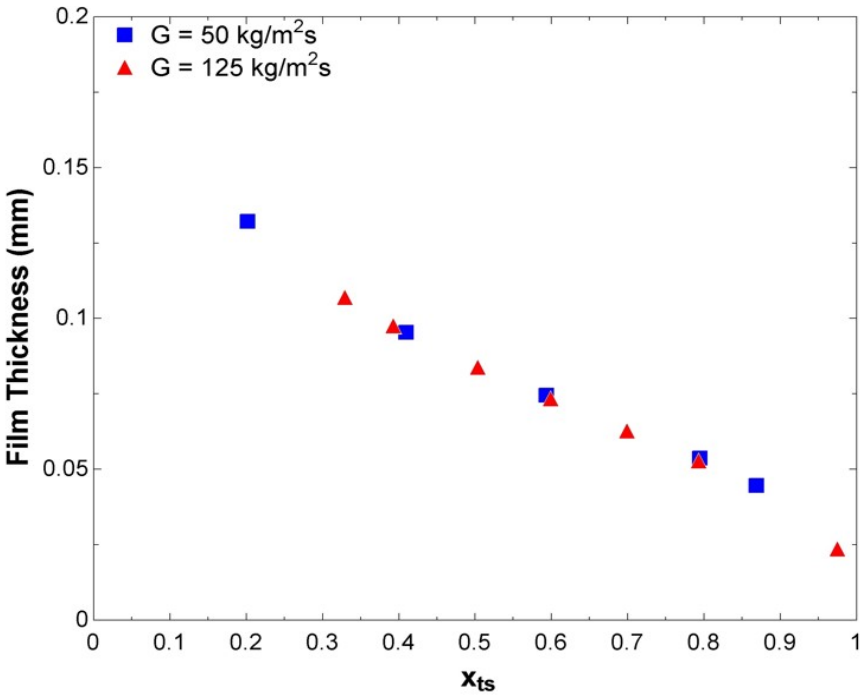

Figure 4.9 Predicted maximum liquid film thickness using the Butterworth [77] void fraction model figure from [1]

In the plain coupon, the thermal resistance is inversely related to the film depth: however, relative to that film depth, the mounds' 1-mm radius proves a significant obstacle to the flow. For low qualities where the film is thickest (e.g., $x \leq 0.4$), these disruptions in the film reduce the film thermal resistance by forcing the flow to either pass over or around the mounds, increasing velocity, and decreasing the relative thickness of the film. For higher qualities (e.g., $x \geq 0.6$), the film is thin enough for the mounds to have direct contact with the vapor, allowing them to act as fins, thereby increasing the condensing surface area and increasing the planform heat transfer coefficient in addition to disrupting the film. For all qualities both the film disruptions and fin effects occur; however, they are most dominate for low and high qualities respectively, which is why for midrange qualities, $0.4 \leq x \leq 0.6$ the lowest enhancement occurs. Based on the liquid film disruptions observed, it stands to reason that there is some optimal grouping of mounds. If the mounds are too far apart, the opportunity for condensation enhancement via film disruption and fin area is missed. However, if the fins are grouped too closely, such as in a hexagonal close pack,

the may thicken due to a smaller effective channel width and the film could also stagnant at the bottom of the channel where the mounds meet, preventing convective heat transfer from locally dominating over conductive heat transfer in the film.

4.3 Porous coupons

Three coupons utilized porous structures made from copper micro-particles. Two had a monolayer of either 100 µm or 200 µm particles sintered along the bottom of the rectangular channel. The other coupon was constructed using 200 µm particles that were sintered to form hemispheres with a 2-mm diameter in the same pattern as in the solid mound coupon. For both types of porous surfaces, the planform area was used to calculate the heat transfer coefficient.

4.3.1 Condensation heat transfer coefficients

For the 100 µm monolayer coupon with a mass flux of 50 kg/m^{2}s, heat transfer coefficients increased in a linear fashion from 26,200 W/m^{2}K to 47,200 W/m^{2}K over qualities from 0.20 to 0.81. The highest quality enhancement occurred at a quality of 0.20 with an enhancement of 20%. For all other heat transfer coefficients at this mass flux, the enhancement was negative, being approximately -10% at a quality 0.40 but increasing in value to -5.2% at a quality of 0.81. For the mass flux of 125 kg/m^{2}s, the heat transfer coefficients began at 49,300 W/m^{2}k and increased to 75,400 W/m^{2}K over qualities from 0.37 to 0.79. The enhancement at this mass flux was 14% for the two lowest qualities tested, 0.37 and 0.40, then decreased in an approximately linear way to an increase of 4.6% at quality of 0.80.

For the 200 µm monolayer coupon with a mass flux of 50 kg/m^{2}s, heat transfer coefficients increased from 33,300 W/m^{2}K to 65,500 W/m^{2}K over qualities from 0.20 to 0.90. The highest quality enhancement occurred at a quality of 0.20 with an enhancement of 52%. For the qualities

of 0.40 to 0.79 the enhancement decreased from 11% to -3.3% before increasing again to 22% at a quality of 0.90. For the mass flux of 125 kg/m^{2}s, the heat transfer coefficients began at 46,000 W/m^{2}k and increased to 100,000 W/m^{2}K over qualities from 0.33 to 0.97. The enhancement at this mass flux was 14% at a quality of 0.33. The maximum enhancement of 16% occurred at a quality of 0.60 before decreasing to 5.6% at a quality of 0.97.

For the 200 µm mound coupon with a mass flux of 50 kg/m^{2}s, heat transfer coefficients increased from 31,000 W/m^{2}K to 44,400 W/m^{2}K over qualities from 0.21 to 0.81. The highest quality enhancement occurred at a quality of 0.21 with an enhancement of 57% and decreases to an enhancement of -6.0% at a quality of 0.71 before increasing to 1.9% at a quality of 0.81. For the mass flux of 125 kg/m^{2}s, the heat transfer coefficients began at 37,300 W/m^{2}k and increased to 79,000 W/m^{2}K over qualities from 0.21 to 0.79. The enhancement at this mass flux was 22% at a quality of 0.21 and decreased to a minimum enhancement of 9.9% at a quality of 0.79. Despite the solid mounds and the 200 µm particle mounds having the same profile, the heat transfer coefficients for the solid mound were consistently higher. This is likely due to the higher effective thermal conductivity of the solid mound coupon. While bother coupons were made via sintering, the porous nature of the 200 µm particle mounds restructure the pathways available for heat transfer and therefore increase the thermal resistance through the structure.

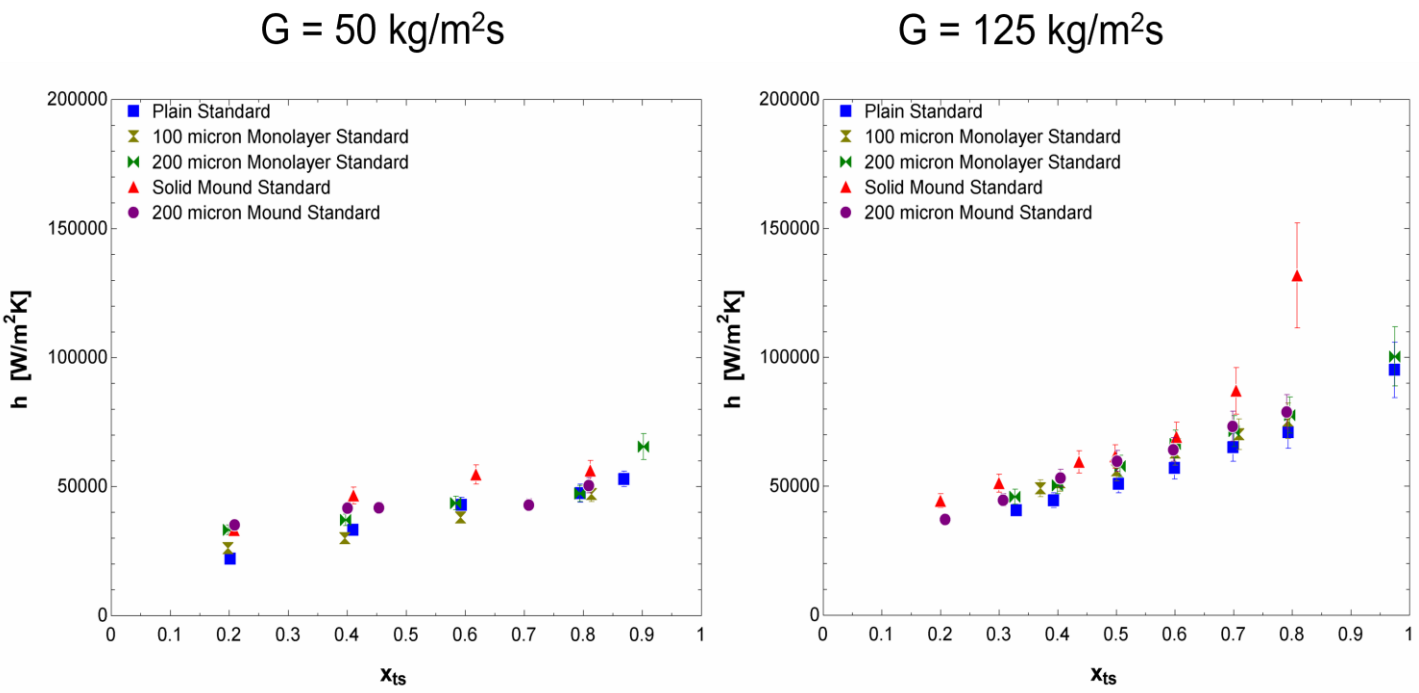

Figure 4.10 Heat transfer coefficients in all hydrophilic coupons tested in standard orientation

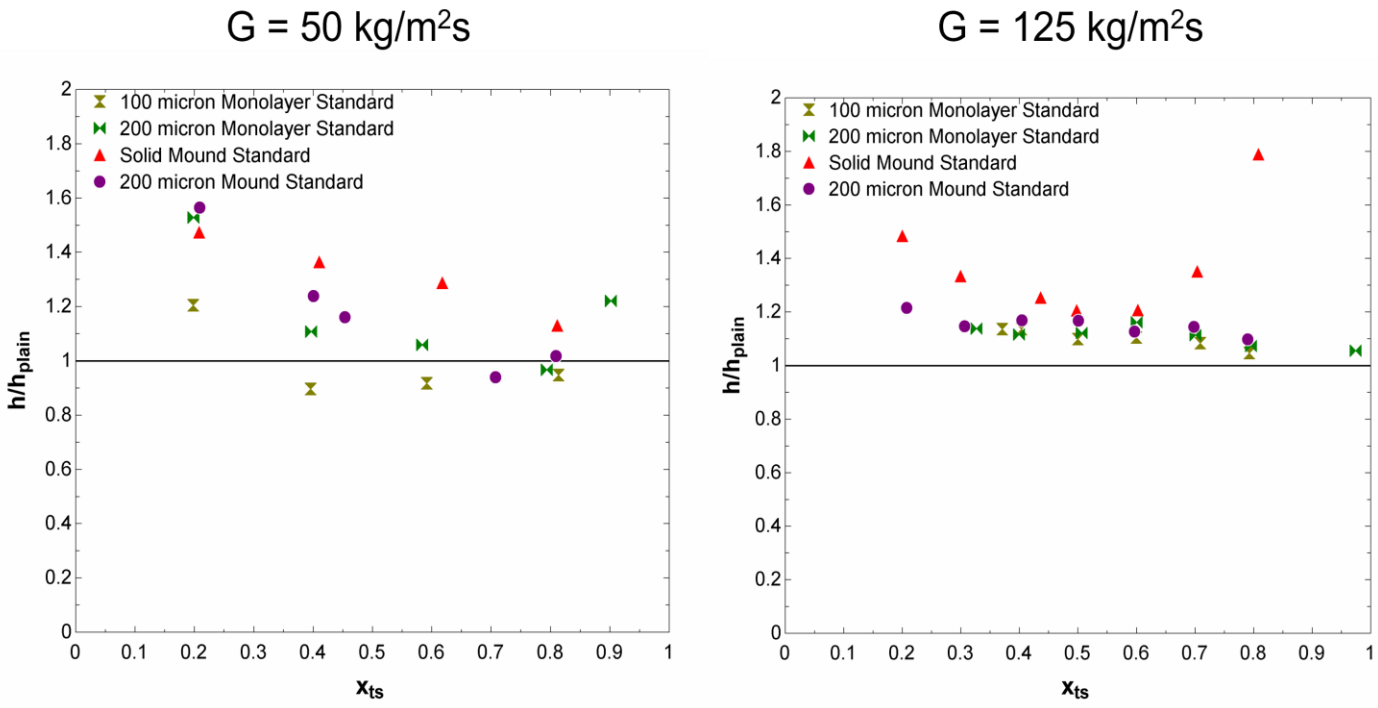

Figure 4.11 Heat transfer coefficient enhancement in all hydrophilic coupons as compared to the plain coupon in standard orientation

4.3.2 Film visualization for porous surfaces

In the monolayer coupons, the presence of micro-particles did cause some level of film disruption, similar to what was seen with the solid mound coupon where ripples and wakes form downstream of the particles. However, due to the small size of the particles, versus the solid mounds, the effects of this did not increase the heat transfer coefficients as greatly or as consistently as the solid mound did. At a mass flux of 50 kg/m^{2}s, the 100 µm monolayer coupon even decreased the heat transfer coefficient compared to the plain coupon for the qualities of 0.40, 0.59, and 0.81, while the 200 µm monolayer coupon at the same mass flux only had a decreased heat transfer coefficient at a quality of 0.79. Likewise, the 200 µm mound coupon at a mass flux of 50 kg/m^{2}s also saw a decrease in heat transfer coefficient at a quality of 0.71. With none of these points occurring in the higher mass flux and low quality, it is likely that the monolayers acted to "trap" the condensate within the structure which reduce the effective thermal conductivity of the monolayer structure. This is similar to the findings of Modak et al. [65], who in gravity driven vertical steam condensation, did not see heat transfer enhancement for any monolayers with particles larger than 50 µm. However, since this study had forced flow, film removal can occur via shear forces at the liquid-vapor interface, which increases convective heat transfer.

For the 200 µm mound coupon, the film was disrupted in much the same way as it was for the solid mound coupon. Despite that, the 200 µm mound coupon did not increase the heat transfer coefficient as much for all but one point in the 50 kg/m^{2}s mass flux. For the mass flux of 125 kg/m^{2}s, the enhancement did not follow the same parabolic shape as the solid mound coupon, though the heat transfer coefficient was increased for all points. At a quality of ~0.8 in the solid mound coupon, the enhancement was 79% while in the 200 µm micron mound coupon it was

9.9%. This difference is best explained by the decreased thermal conductivity of the sintered mound.

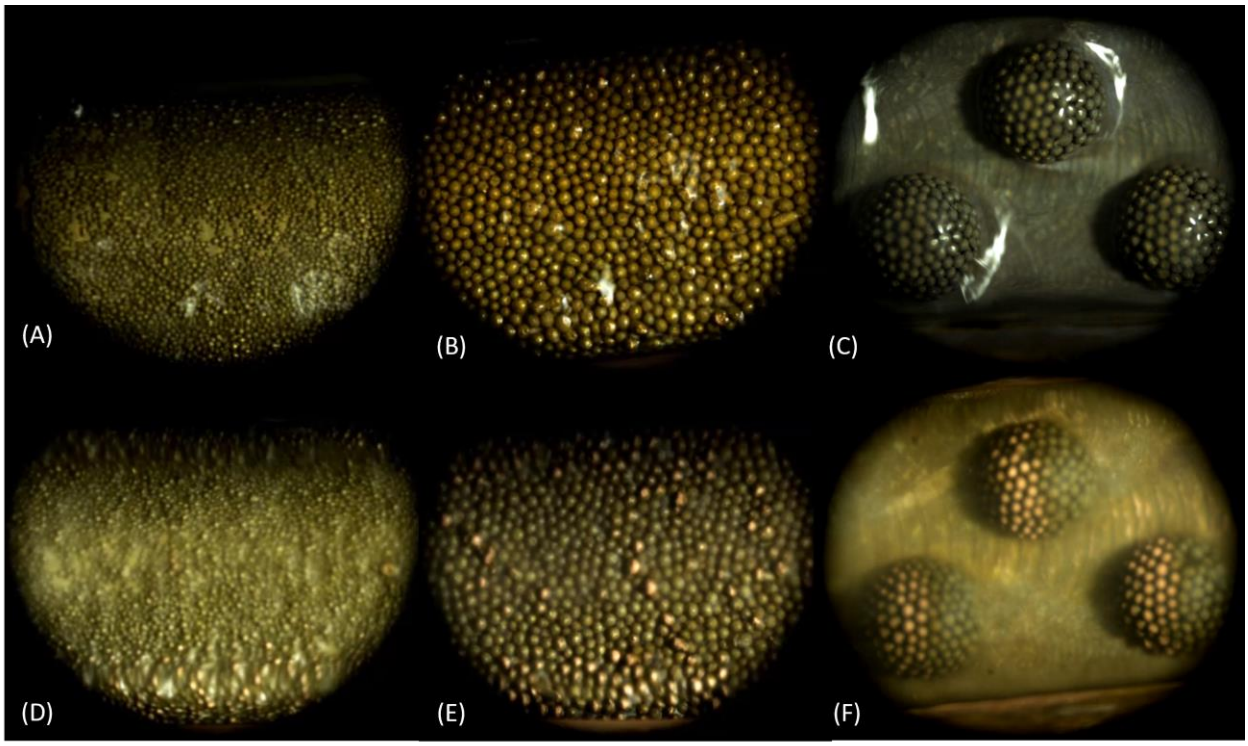

Figure 4.12 Films in porous coupon in standard orientation with a quality of 0.6 at: (A) a mass flux of 50 kg/m^{2}s in the 100 µm monolayer coupon, (B) a mass flux of 50 kg/m^{2}s in the 200 µm monolayer coupon, (C) a mass flux of 50 kg/m^{2}s in the 200 µm mound coupon, (D) a mass flux of 125 kg/m^{2}s in the 100 µm monolayer coupon, (E) a mass flux of 125 kg/m^{2}s in the 200 µm monolayer coupon, (F) a mass flux of 125 kg/m^{2}s in the 200 µm mound coupon

4.4 Pressure drops

For the plain coupon with a mass flux of 50 kg/m^{2}s, the pressure drops ranged from 1.8 kPa to 8.8 kPa for qualities from 0.20 to 0.87. At a mass flux of 125 kg/m^{2}s, the pressure drops ranged from 15 kPa to 92 kPa for qualities from 0.33 to 0.97. For the monolayer coupons, the pressure drops were not significantly different than for the plain coupon. For the 100 µm monolayer with a mass flux of 50 kg/m^{2}s, the pressure drop varied from 1.3 kPa to 6.9 kPa for qualities from 0.20 to 0.81. For a mass flux of 125 kg/m^{2}s, the pressure drop ranged from 20 kPa to 63 kPa for qualities from 0.37 to 0.79. For the 200 µm monolayer coupon, with a mass flux of

50 kg/m^{2}s the pressure drop varied from 0.85 kPa to 8.8 kPa for qualities from 0.20 to 0.90. For a mass flux of 125 kg/m^{2}s, the pressure drop ranged from 14 kPa to 88 kPa for qualities from 0.33 to 0.97. The Reynolds number for the liquid phase, Re_l was calculated using the following equation:

$$Re_l = G(1-x)D_h \quad \textbf{4.5}$$

to find that the largest liquids Reynolds number, occurring for a mass flux of 125 kg/m^{2}kg and a quality of 0.31, for the film was 749, well below the laminar-turbulent boundary. Due to being laminar, the surface roughness effects that the monolayer would have in a turbulent flow do not impact the pressure drop as seen in Figure 4.13.

The mound coupons experienced greater pressure drops than the plain and monolayer coupons though similarly, the porous mound coupon did not have a significant difference in pressure drops compared to the solid mound coupon, due to the laminar film. For the solid mound coupon at a mass flux of 50 kg/m^{2}s, the pressure drops were 1.2 kPa to 9.2 kPa for qualities from 0.21 to 0.81. For the mass flux of 125 kg/m^{2}s, the pressure drop varied from 10 kPa to 114 kPa at qualities of 0.20 to 0.81. In the 200 µm mound coupon, with a mass flux of 50 kg/m^{2}s, the pressure drops were 3.1 kPa to 8.6 kPa for qualities from 0.21 to 0.81. For the mass flux of 125 kg/m^{2}s, the pressure drops varied from 11 kPa to 95 kPa at qualities of 0.21 to 0.79.

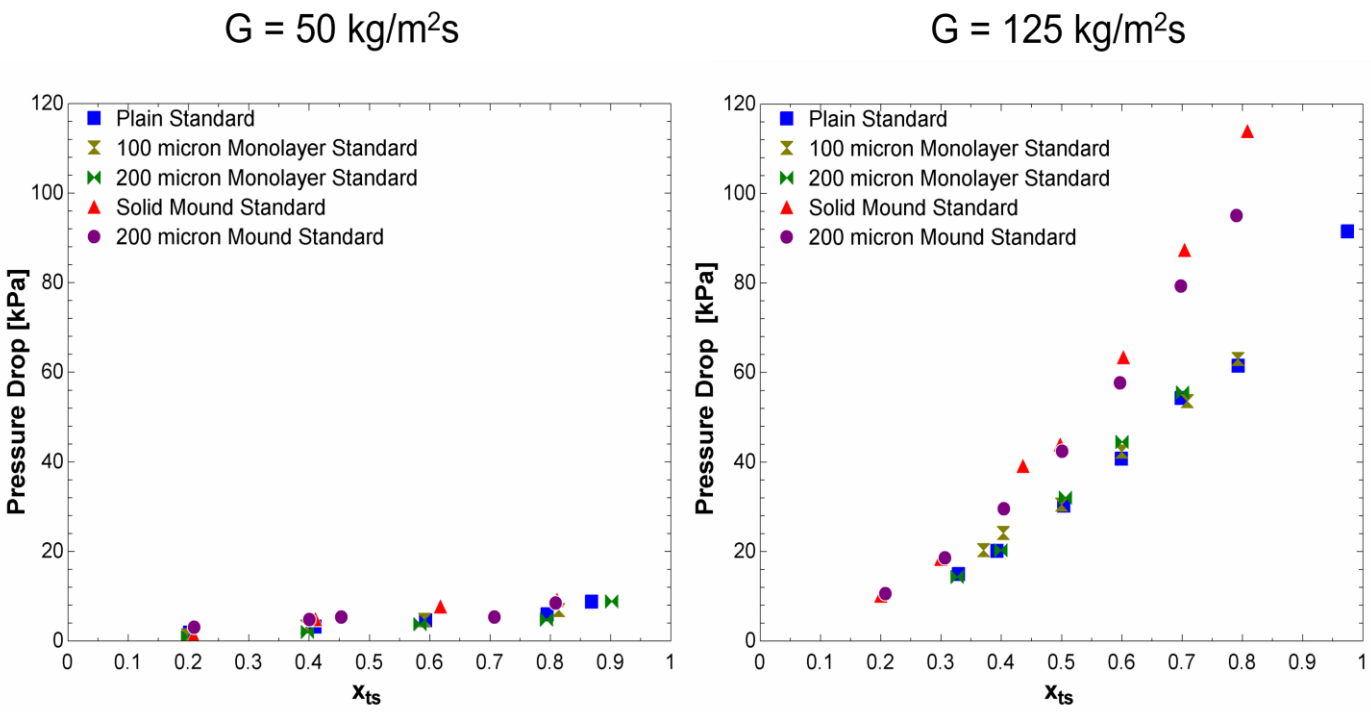

Figure 4.13 Pressure drop for all hydrophilic coupons in standard orientation

Chapter - 5 Filmwise condensation in the inverted orientation

In order to understand the impacts of gravity, the test section was inverted (i.e., experiencing upper surface condensation, where gravity pulls the film away from the condensing surface).

5.1 Condensation heat transfer coefficients

Flow condensation data for the inverted test sections, where condensation occurred on the upper surface, had similar results to that of the standard test sections. For the plain inverted test section, at a mass flux of 50 kg/m^{2}s, heat transfer coefficients ranged from 23,700 W/m^{2}K to 47,000 W/m^{2}K at qualities from 0.20 to 0.87, which corresponded to an increase of 6.8% and a decrease of 10% in heat transfer coefficients, respectively. At a mass flux of 125 kg/m^{2}s, the plain inverted test section had heat transfer coefficients from 37,300 W/m^{2}K to 62,000 W/m^{2}K at qualities from 0.34 to 0.79. In this case there was no heat transfer enhancement, with a decrease in performance of 9.5% at a quality of 0.34 to a decrease of 14% at a quality of 0.79. The minimum decrease in heat transfer coefficient was 2.2% and occurred at a quality of 0.51. For the inverted plain test section, all decreases in heat transfer coefficient were less than 10%.

For the inverted mound test sections at a mass flux of 50 kg/m^{2}s, heat transfer coefficients ranged from 37,300 W/m^{2}K to 74,800 W/m^{2}K at qualities of 0.23 and 0.90 respectively with corresponding enhancements of 56% to 40% with a low of 37% occurring at a quality of 0.56. With a mass flux of 125 kg/m^{2}s, the heat transfer coefficients went from 42,300 W/m^{2}K to 110,000 W/m^{2}K at qualities from 0.21 to 0.80. As with the standard orientation, the enhancement was parabolic with an enhancement of 38% at quality of 0.21 and 51% at a quality of 0.80. The lowest enhancement was 27% and occurred at a quality of 0.61 where the film was not thick enough to

be significantly impacted by the presence of mounds nor so thin that the mounds protruded above the film.

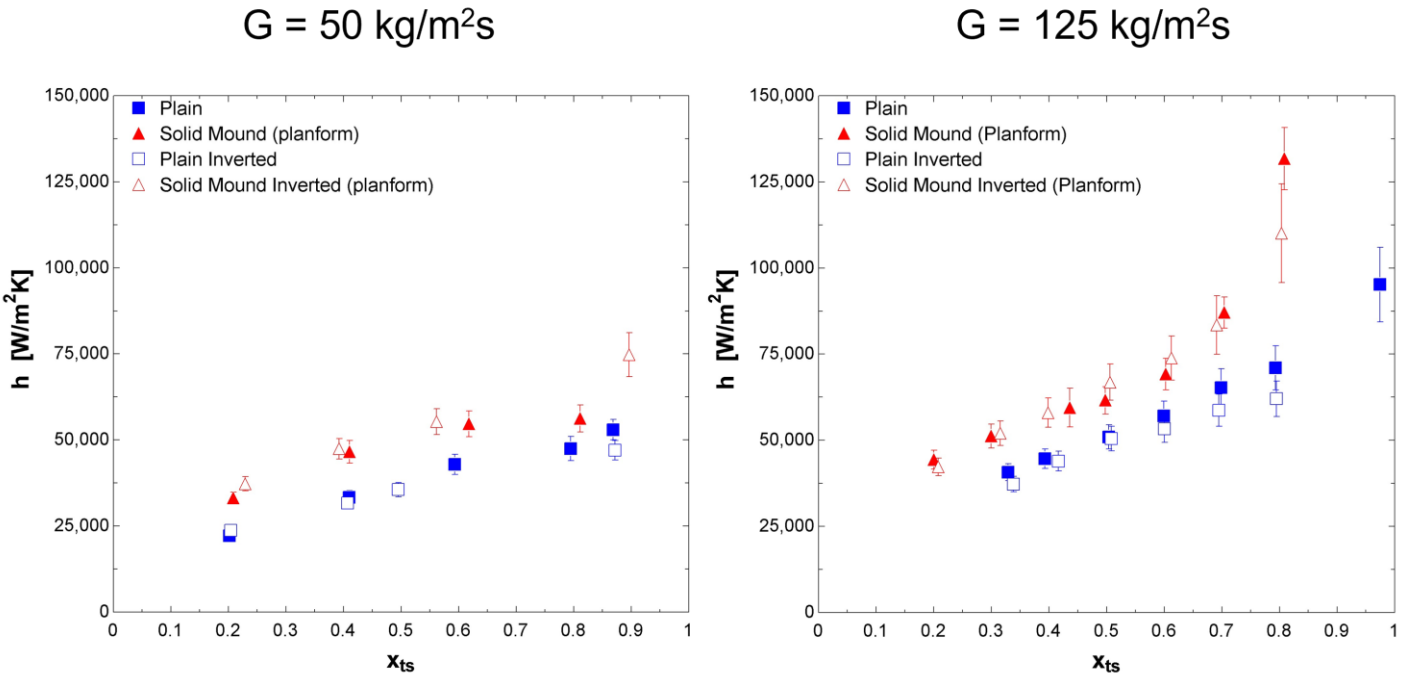

Figure 5.1 Heat transfer coefficients for the plain and solid mound coupons in standard and inverted orientations figure from [1]

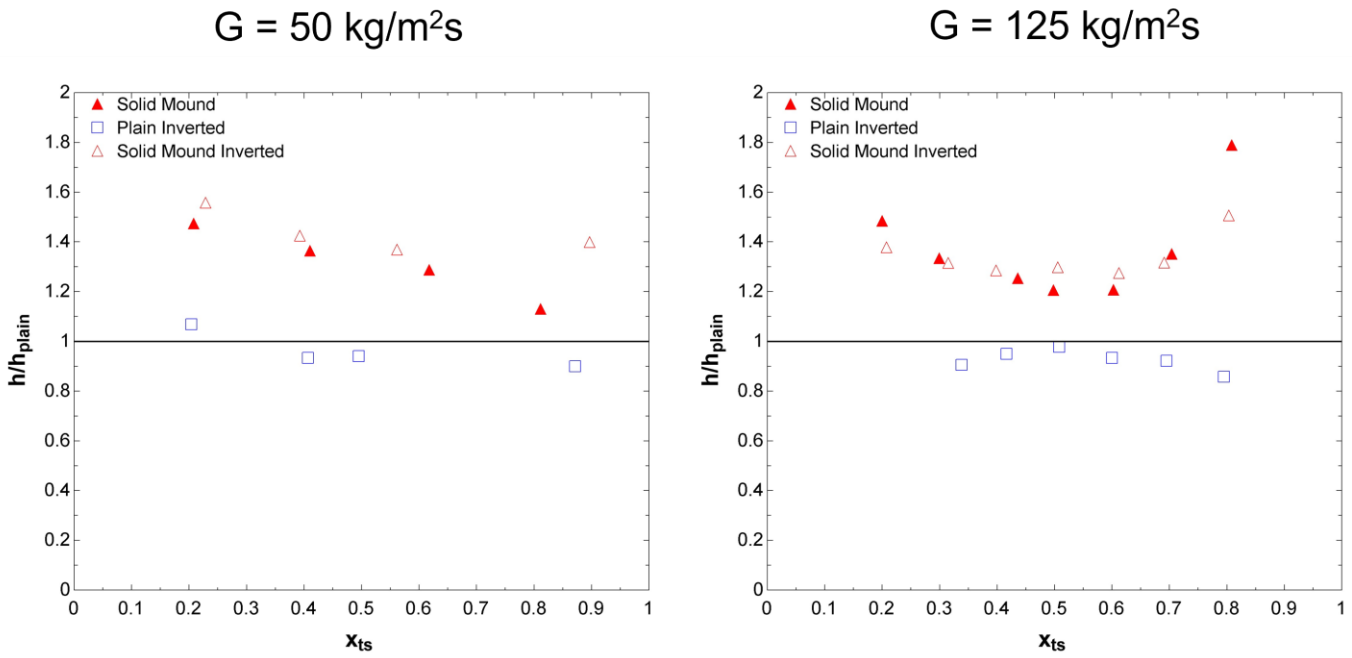

Figure 5.2 Heat transfer coefficient enhancements for the plain and solid mound coupons in standard and inverted orientations figure from [1]

5.2 Flow regime analysis

For both coupons, the inversion of the test section had little visual impact on the film, which continued to flow in contact with the cooling surface as described in sections 4.1.3 and 4.2.2, despite that being the upper side of the flow channel for both mass fluxes and all qualities observed. Figure 5.3 shows the flow regimes for the plain and solid mound coupons in both orientations for a quality of 0.6 and both mass fluxes.

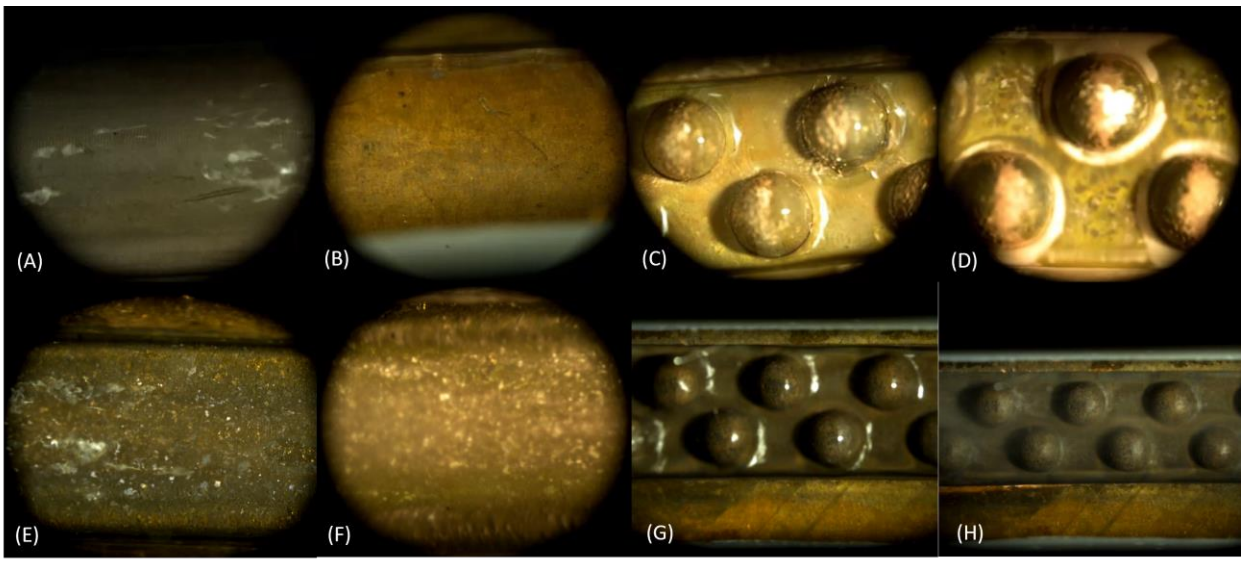

Figure 5.3 Standard and inverted films in the plain and solid mound coupons with a quality of 0.6; (A) standard plain coupon with a mass flux of 50 kg/m^{2}s, (B) standard plain coupon with a mass flux of 125 kg/m^{2}s, (C) standard mound coupon with a mass flux of 50 kg/m^{2}s, (D) standard mound coupon with a mass flux of 125 kg/m^{2}s, (E) inverted plain coupon with a mass flux of 50 kg/m^{2}s, (F) inverted plain coupon with a mass flux of 125 kg/m^{2}s, (G) inverted mound coupon with a mass flux of 50 kg/m^{2}s, (H) inverted mound coupon with a mass flux of 125 kg/m^{2}s

The heat transfer performance was also not significantly impacted by gravity and thus, two nondimensional numbers were evaluated to explain the phenomena. The Eötvös number, *Eo*, which represents the ratio of gravitational to surface tension forces, was calculated [22],

$$Eo = gD_h^2 \frac{(\rho_l - \rho_g)}{\sigma} \quad \textbf{5.1}$$

where g is the gravity constant, D_h is the hydraulic diameter, and σ is the surface tension. The Eötvös number was 0.64 and 0.60 for the plain and mound coupons, respectively. Eötvös numbers less than one support that gravitation forces are not dominant in these coupons. The modified Weber number, We^*, which represents the ratio of inertial to surface tension forces, was employed to determine the expected flow regime for each data point [21],

$$We^* = \frac{2.45Re_g^{0.64}}{Su_g^{0.3}(1 + 1.09X_{tt}^{0.039})^{0.4}} \quad \textbf{5.2}$$

$$Re_g = \frac{G(1-x)D_h}{\mu_l} \quad \textbf{5.3}$$

$$Su_g = \frac{\rho_g \sigma D_h}{\mu_g^2} \quad \textbf{5.4}$$

$$X_{tt} = \left(\frac{\mu_l}{\mu_g}\right)^{0.1} \left(\frac{1-x}{x}\right)^{0.9} \left(\frac{\rho_g}{\rho_l}\right)^{0.5} \quad \textbf{5.5}$$

where Re_g is the Reynolds number of the gas phase, Su_g is the Suratman number of the gas phase, G is the mass flux of steam, and X_{tt} is the Lockhart-Martinelli parameter. The primary difference between these flow regimes being the presence of a consistent vapor core in the wavy-annular flow while slug flow; the vapor forms long bubbles separated by periods where the film fills the entire cross-sectional area. For all flow regimes other than stratified flow, the film covers the entire condensing surface. The boundary between wavy-annular and transitional flows is defined by $We^* = 24X_{tt}^{0.41}$ and the boundary between transitional and slug flow is $We^* = 90X_{tt}^{02}$. The results can be seen in Figure 5.4 and shows the flow regimes are expected to be either slug flow, transitional (between slug and annular), or wavy-annular flow; few data are in the slug flow regime. This

supports the observed behavior for the film to adhere to the copper surface regardless of orientation as for these flow regimes the film wet the entire channel surface.

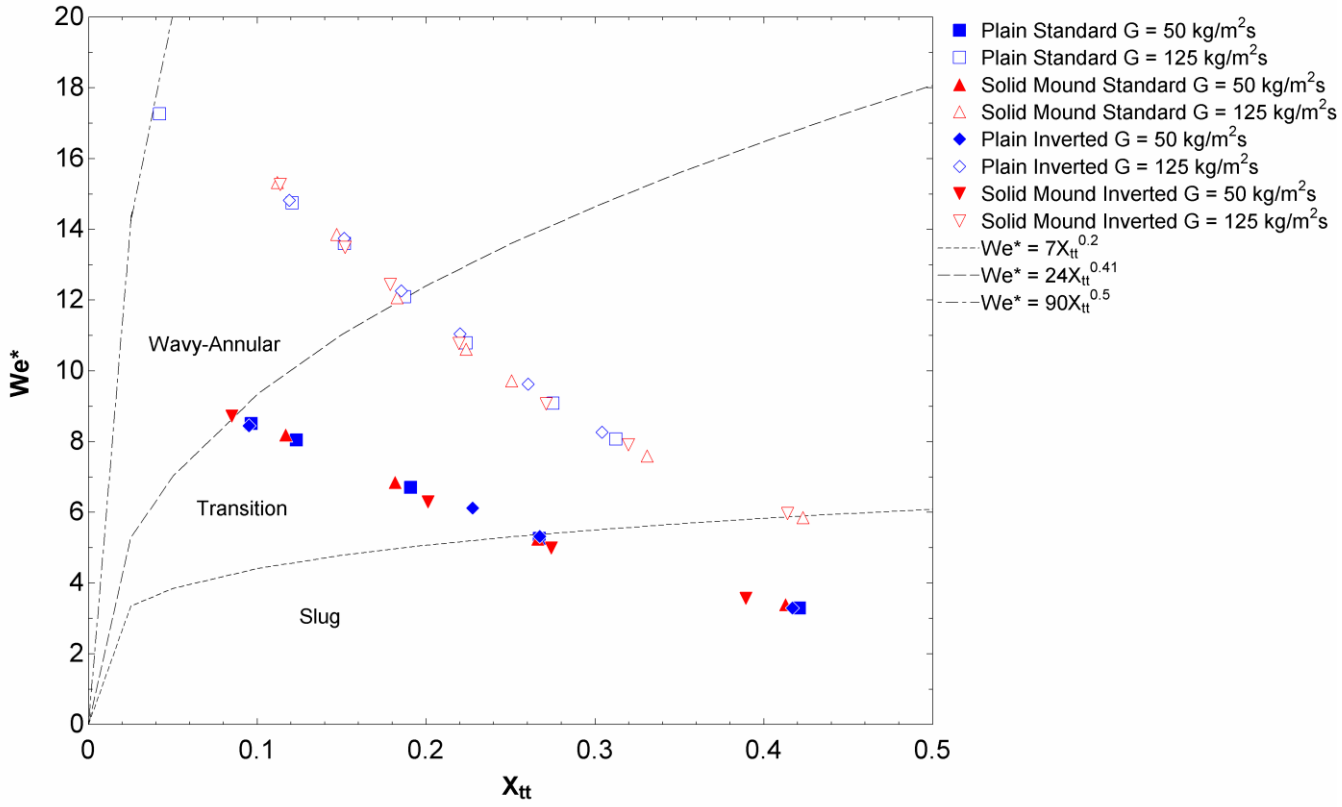

Figure 5.4 Flow regimes for the plain and solid mound coupons in both standard and inverted orientations figure from [1]

5.3 Pressure drops

Pressure drops were parabolic for both coupons and orientations and were increased with quality and mass flow rate. The pressure drops in the solid mound coupon were also higher; however, changing the orientation of the test section had minimal impacts, as shown in Figure 5.5. For the plain coupon with a mass flux of 50 kg/m^{2}s, the pressure drops ranged from 1.8 kPa to 8.8 kPa for qualities from 0.20 to 0.87. At a mass flux of 125 kg/m^{2}s, the pressure drops ranged from 15 kPa to 92 kPa for qualities from 0.33 to 0.97. When the test section was inverted, at the mass flux of 50 kg/m^{2}s pressure drops went from 1.8 kPa to 9.9 kPa for qualities from 0.20 to 0.87 and

from 16 kPa to 67 kPa for qualities from 0.34 to 0.79. The standard mound coupon at 50 kg/m^{2}s had pressure drops from 1.2 kPa to 9.2 kPa for qualities from 0.21 to 0.81. At a mass flux of 125 kg/m^{2}s pressure drops ranged from 10 kPa to 110 kPa for qualities from 0.20 to 0.81. For the inverted mound coupon at 50 kg/m^{2}s pressure drops ranged from 3.1 kPa to18 kPa for qualities from 0.23 to 0.90 and at a mass flux of 125 kg/m^{2}s the pressure drops were from 11 kPa to 120 kPa for qualities from 0.21 to 0.80.

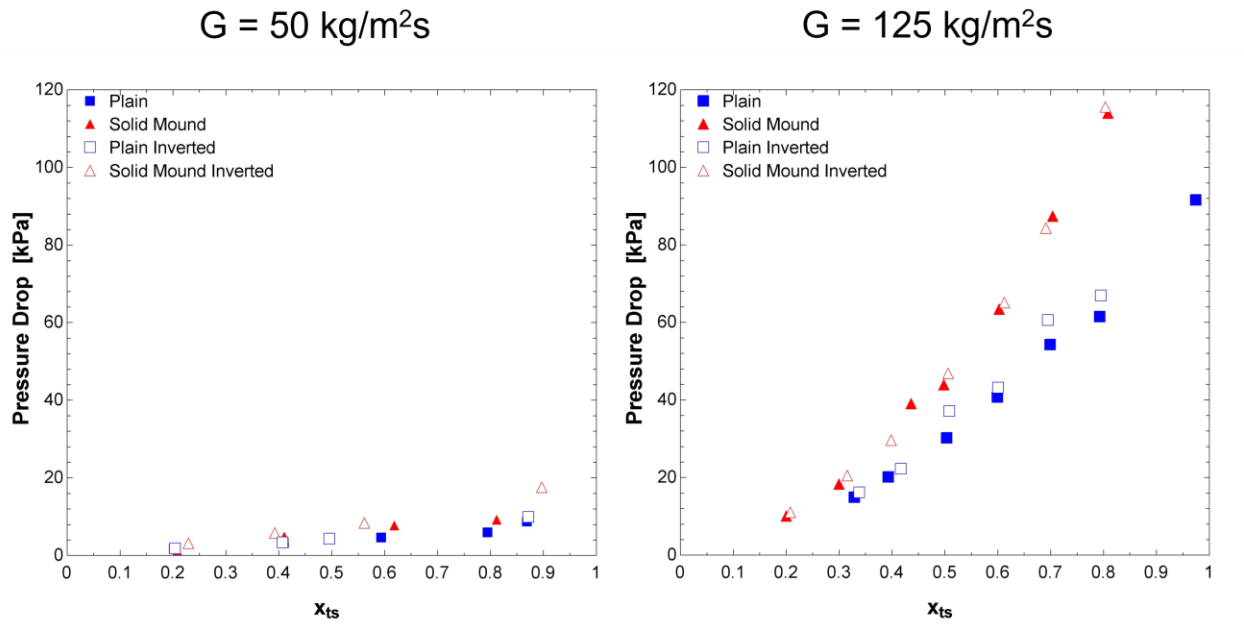

Figure 5.5 Pressure drops in the plain and solid mound coupons in standard and inverted orientation figure from [1]

Chapter - 6 Dropwise Condensation

6.1 Teflon coating process

In order to evaluate the effects of channel orientation during dropwise condensation, the plain coupon was coated with Teflon AF^{TM} which increased its contact angle to 110 ± 3° from the uncoated copper surface which had a contact angle of 70 ± 3°. To coat the coupon, the surface was initially cleaned in acetic acid to remove any copper oxide, placed in a vacuum chamber for 8 hours to completely dry, placed in a UV cleaner (ProCleaner^{TM} 110) for 30 minutes to remove contaminants, then soaked in isopropanol for 10 minutes to remove any remaining particles. The coupon was then dipped twice into a solution of Teflon AF^{TM} 1601 x 6% mixed with FC40 at a ratio of 1:20. The coupon was then baked at 120 °C for three hours to set the Teflon, then baked at the glass transition temperature of 165 °C for 72 hours to create a uniform coating. At the end of this process, the coupon was visually inspected for any delamination or plate formation. The coupon was baked a third time at 180 °C for an additional 72 hours. After this, the coupon was visually inspected again, tested with a water drop to verify hydrophobicity, and deemed acceptable for heat transfer experiments.

6.2 Heat transfer coefficients

In filmwise condensation, the condensate film forms a layer on the condensing surface that acts as a thermal barrier. In dropwise condensation, no such film occurs as the condensate is removed from the condensing surface before the nucleating drops can grow large enough to merge and form a film across the surface, which allows for significantly higher heat transfer coefficients. Chen and Derby [9] determined that for a coupon with a hydraulic diameter 0.952 mm, the steam heat transfer coefficient increased 480%-614% for mass fluxes of 50 kg/m^{2}s, 75 kg/m^{2}s, and 100

kg/m^{2}s by inducing dropwise condensation. Data for this study are presented for the hydrophobic plain coupon in both standard and inverted orientations.

For the hydrophobic plain coupon in the standard orientation with a mass flux of 50 kg/m^{2}s, the heat transfer coefficient ranges 87,00 W/m^{2}K to 142,000 W/m^{2}K for qualities from 0.18 to 0.79, where the heat transfer coefficient changes by less than 0.3% between the qualities of 0.52 and 0.79. When the mass flux is 125 kg/m^{2}s the heat transfer coefficients range from 110,000 W/m^{2}K to 536,000 W/m^{2}K for qualities from 0.20 to 0.78. For this mass flux and higher qualities, the difference in temperature between the two-phase steam and the surface of the coupon becomes very small, as low as 0.3 °C for the mass flux of 125 kg/m^{2}s and a quality of 0.78 as compared to a more typical difference of 5 °C – 16.4 °C for the hydrophilic plain coupon. This caused the uncertainty in the calculated value for the heat transfer coefficient to increase significantly, reaching an uncertainty of 179% the value of the heat transfer coefficient for the quality of 0.78. Despite this large uncertainty for these cases due to the small fluid-wall temperature differences, the data are included since available experimental steam condensation data is limited for mini-channels. The corresponding heat transfer coefficient enhancements for the standard orientation hydrophobic coupon at a mass flux of 50 kg/m^{2}s decrease linearly from 320% to 190% over the quality ranges of 0.18 to 0.79. For the mass flux of 125 kg/m^{2}s, the enhancement increases with quality, from an enhancement of 260% to 660% for qualities from 0.20 to 0.78.

In the inverted orientation, with a mass flux of 50 kg/m^{2}s, the heat transfer coefficients have a weaker correlation to quality, varying from 124,000 W/m^{2}K to 144,000 W/m^{2}K for qualities from 0.19 to 0.69 where the highest heat transfer coefficient of 158,000 W/m^{2}K at a quality of 0.50. For the mass flux of 125 kg/m^{2}s, the heat transfer coefficients increase with quality from 174,000 W/m^{2}K to 774,000 W/m^{2}K for qualities from 0.22 to 0.78. As with the standard

orientation case, the uncertainties increase as the temperature difference between the condensing surface the steam decreases reaching a maximum uncertainty of 163% at a quality of 0.78. The heat transfer coefficient enhancements for the inverted case for a mass flux of 50 kg/m^{2}s decrease linearly from 480% to 220% for the qualities of 0.19 to 0.69. At a mass flux of 125 kg/m^{2}s, the heat transfer coefficient enhancements vary from 460% to 990% with a minimum enhancement of 370% at a quality of 0.40.

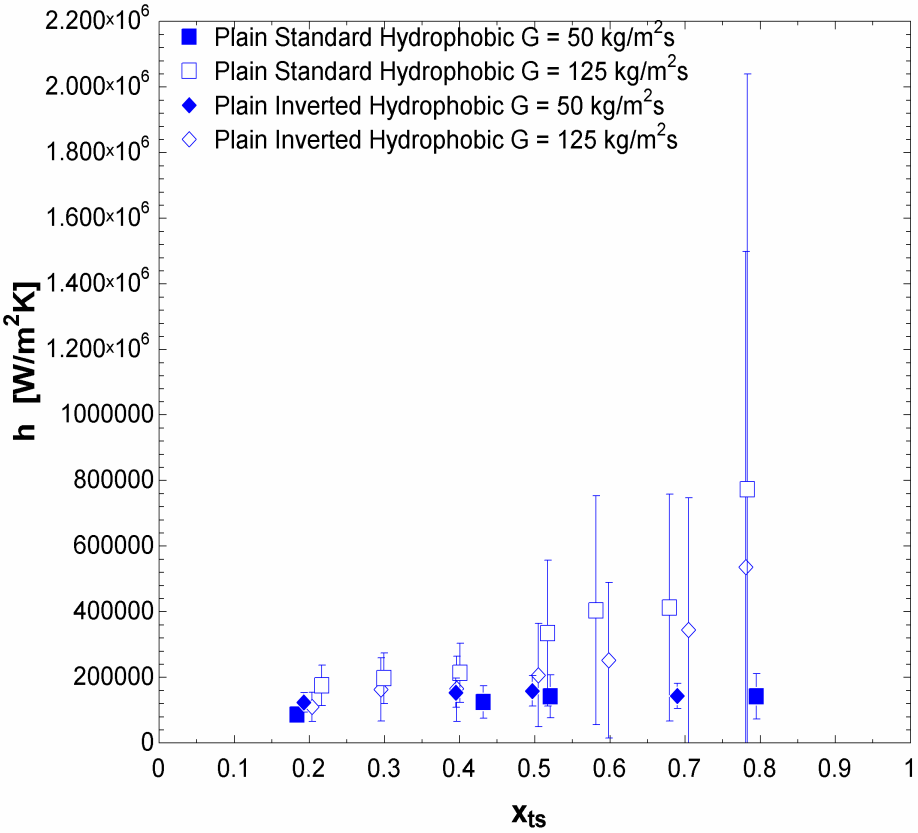

Figure 6.1 Heat transfer coefficients for the hydrophobic plain coupon in standard and inverted orientations

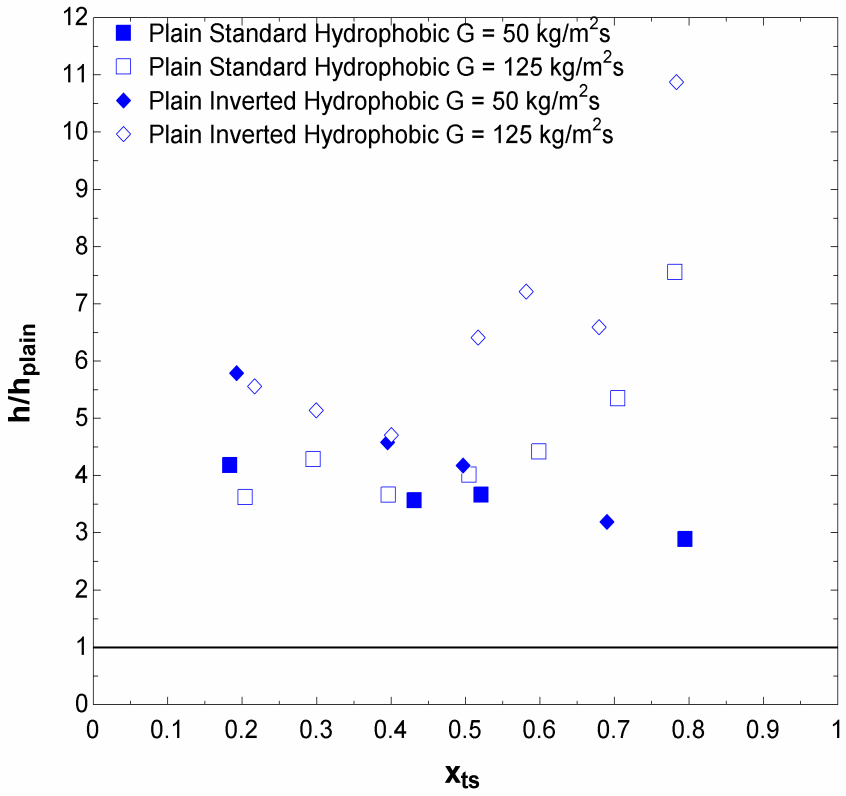

Figure 6.2 Heat transfer enhancements for the hydrophobic plan coupon in plain and standard orientation

6.3 Flow visualization for hydrophobic plain coupons

With the hydrophobic plain coupon, the condensation is no longer filmwise as it was for the hydrophilic coupons. Instead, as droplets condense on the surface, they are cleared either by the shear force of the steam pulling them off of the surface or by joining a rivulet of condensate flowing over a portion of the condensing surface. In the standard orientation, but of these processes occur and can be seen in Figure 6.3. In the inverted orientation there were no visible droplets nor a film flowing across the condensing surface. The lack of visible droplets on the suggests that they were too small to be with available camera and lighting. There was, however, condensation flowing across the borosilicate glass slide used for visualizing the condensing surface. Due to the hydrophilic nature of the borosilicate glass, with a contact angle of 11°, any condensate that was not caught in the steam flow would adhere to the glass.

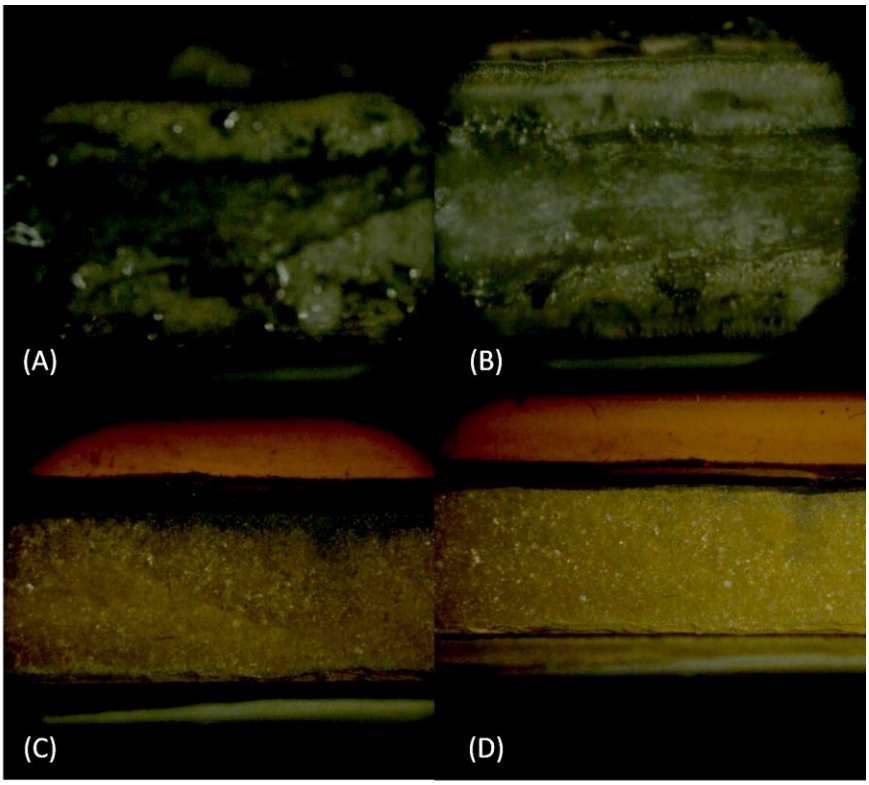

Figure 6.3 Condensate on the hydrophilic plain coupon: (A) standard orientation mass flux of 50 kg/m^{2}s and quality of 0.8, (B) standard orientation mass flux of 125 kg/m^{2}s and quality of 0.8, (C) inverted orientation mass flux of 50 kg/m^{2}s and quality of 0.6, (D) inverted orientation mass flux of 125 kg/m^{2}s and quality of 0.6

6.4 Droplet force analysis

A droplet force balance, shown in Figure 6.4 was created to understand the forces on droplets, and particularly to understand the impacts of departure droplets size in the inverted hydrophobic case. A force balance on a pinned droplet was conducted and shows that the maximum droplet size does decrease when the test section is inverted. In the standard orientation, a pinned droplet experiences a drag force from the steam flow, a lateral adhesive force which is equal in magnitude to the drag force but in the opposing direction. While the base of the droplet is pinned due to the lateral adhesive force, the droplet is distorted by the drag force, creating advancing and receding contact angles. The gravitational force is also present and keeps the droplet on the condensing surface in the standard orientation. When the surface is inverted, a normal adhesive force is required to counteract the gravitational force and keep the droplet pinned to the surface.

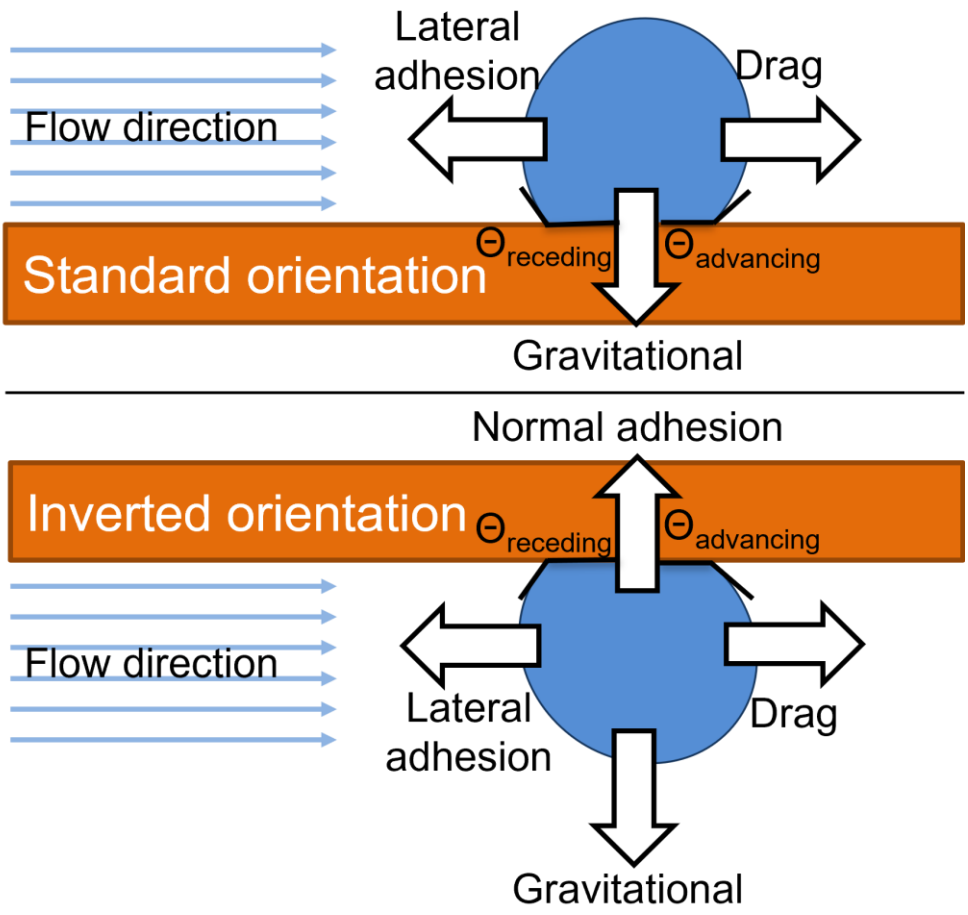

Figure 6.4 Forces acting on a pinned droplet in the standard orientation (top) and inverted orientation (bottom)

In the inverted case, where there are both lateral and normal components to the adhesive force, it is important to note that they both contribute to the total adhesive force of the pinned droplet such that:

$$F_{lateral\ adhesive} = F_{drag} \quad \textbf{6.1}$$

$$F_{normal\ adhesive} = F_{gravity} \quad \textbf{6.2}$$

$$F_{total\ adhesive} = \sqrt{F_{lateral\ adhesive}^2 + F_{normal\ adhesive}^2} \quad \textbf{6.3}$$

where $F_{lateral\ adhesive}$ is the lateral adhesive force keeping the droplet stationary, F_{drag} is the drag force from vapor flow over the droplet, $F_{normal\ adhesive}$ is the adhesive force which prevents the droplet from being lifted off the surface, and $F_{gravity}$ is the gravitational force which will be acting to either pull the droplet off of the surface when in the inverted orientation or keep it on the surface in standard orientation. $F_{total\ adhesive}$ is the combined magnitude of the adhesive forces acting on the droplet.

In order to the determine the magnitude of these forces, the model proposed by Roisman et. al [78] was used to determine the lateral adhesive force as well as the critical depinning force for a droplet through combining equations 6.4 and 6.7,

$$F_{drag} = \rho \left(\frac{dU}{dZ}\right)^2 \frac{H^2 A}{8} \quad \textbf{6.4}$$

$$\frac{dU}{dZ} \approx 0.332 \sqrt{\frac{U_a^3}{\nu L/2}} \quad \textbf{6.5}$$

$$U_a = \frac{Gx\alpha}{\rho_v} \quad \textbf{6.6}$$

$$\left(\frac{dU}{dZ}\right)_{crit} = 4\left[\frac{R\gamma}{\rho H^2 A}\left(cos\theta_{receding} - cos\theta_{advancing}\right)\right]^{1/2} \quad \textbf{6.7}$$

$$F_{gravity} = gV\rho_l \quad \textbf{6.8}$$

where dU/dZ is the vapor velocity gradient in normal direction surface, U_a is the average vapor velocity, H is the height of the droplet, R is the radius of the droplet where it is contact with the surface, A is the projected area of the droplet normal to the vapor flow direction, V is the volume of the droplet, and L is the channel length. Since the droplets are assumed to be small, with diameters smaller than the capillary length of 2.4 mm for liquid water at test conditions, the

geometric properties are approximated by using that of a truncated sphere where the contact angle, Θ, is the average of the advancing and receding contact angles. The critical depinning force is determined by applying equation 6.6 to equation 6.4 and is a function of R, v, and the contact angles.

In Figure 6.5 and Figure 6.6 Forces acting on a stationary droplet for a mass flux of 125 kg/m^2 and a quality of (A) 0.3, (B) 0.8 the drag force, gravitational force, and total adhesive force are plotted with the critical depinning force for a mass flux of 50 kg/m^{2}s and 125 kg/m^{2}s respectively. The maximum possible droplet size for inverted cases occurs where the total adhesive force intersects the critical depinning force. For standard orientation, since $F_{normal\ adhesive}$ is 0, the maximum predicted droplet size occurs where F_{drag} is equal to the critical depinning force. Since the gravitational and critical depinning forces are not dependent on the flowrate or quality, they remain identical for the four flow conditions shown. However, the drag force varies significantly between each case as it increases as a function of both mass flux and quality. The greatest change in maximum stationary droplet size occurred for the lower qualities for both mass fluxes. Where for a quality of 0.2 and a mass flux of 50 kg/m^{2}s, the maximum droplet size decreased by 13.5% from 1.44 mm in standard orientation to 1.25 mm in the inverted orientation. For the same mass flux at a quality of 0.7, the droplet size decreased by 3.8% from 1.00 mm in the standard orientation to 0.96 mm for the inverted orientation. At the higher mass flux of 125 kg/m^{2}s and a quality of 0.2, the droplet size decreased by 10.8% from 1.35 mm in the standard orientation to 1.20 mm in the inverted orientation. In the final case, with a mass flux of 125 kg/m^{2}s and a quality of 0.8, the maximum droplet size decreased by 1.8% from 0.82 mm in the standard orientation to 0.81 mm in the inverted orientation. The decreased maximum droplet size for inverted cases at low quality, $x < 0.5$, provides an explanation for the increased heat transfer coefficient enhancement observed.

Due to smaller droplet sizes at depinning, a greater portion of the condensing surface is available for further condensation.

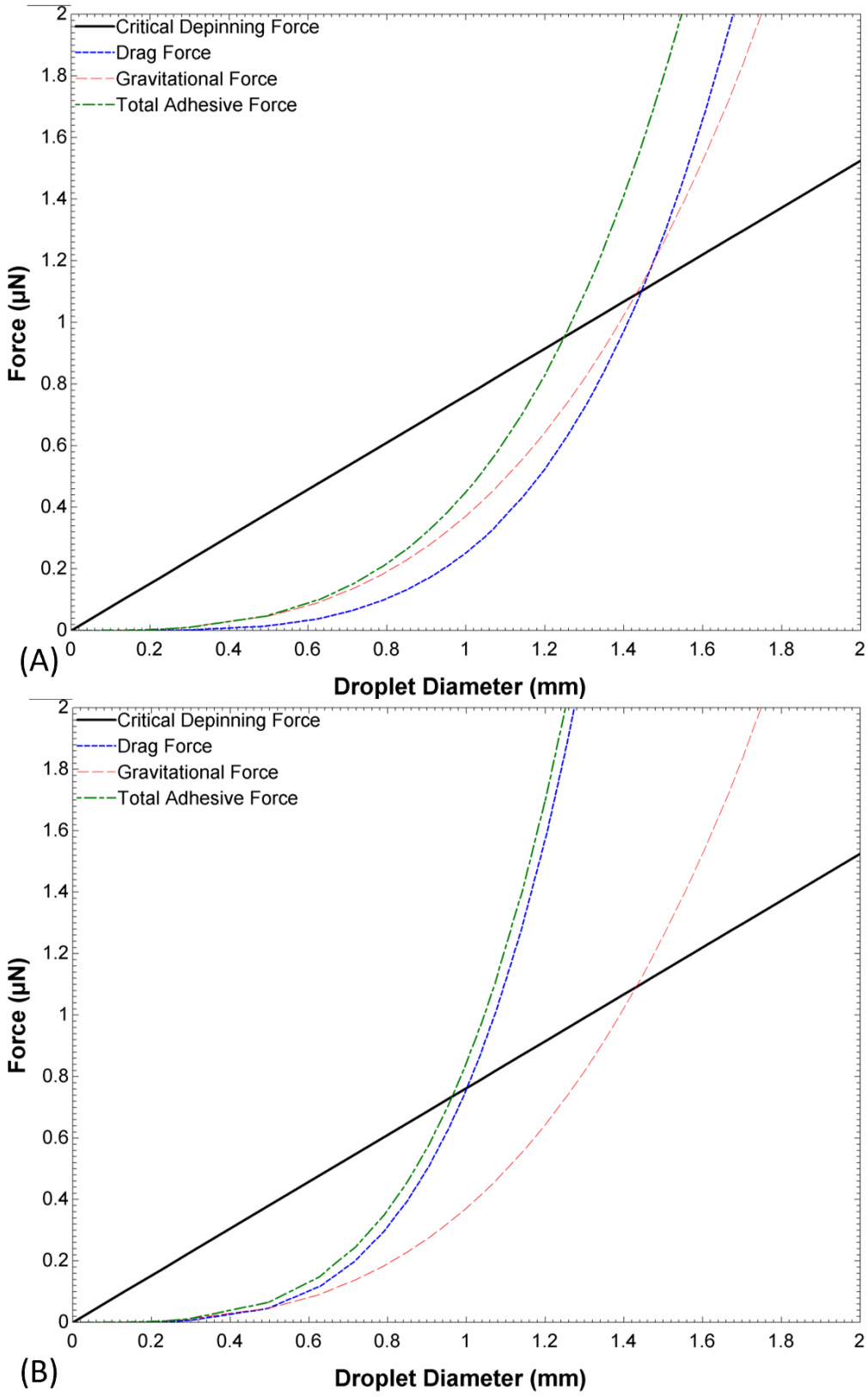

Figure 6.5 Forces acting on a stationary droplet for a mass flux of 50 kg/m^2 and a quality of (A) 0.2, (B) 0.7

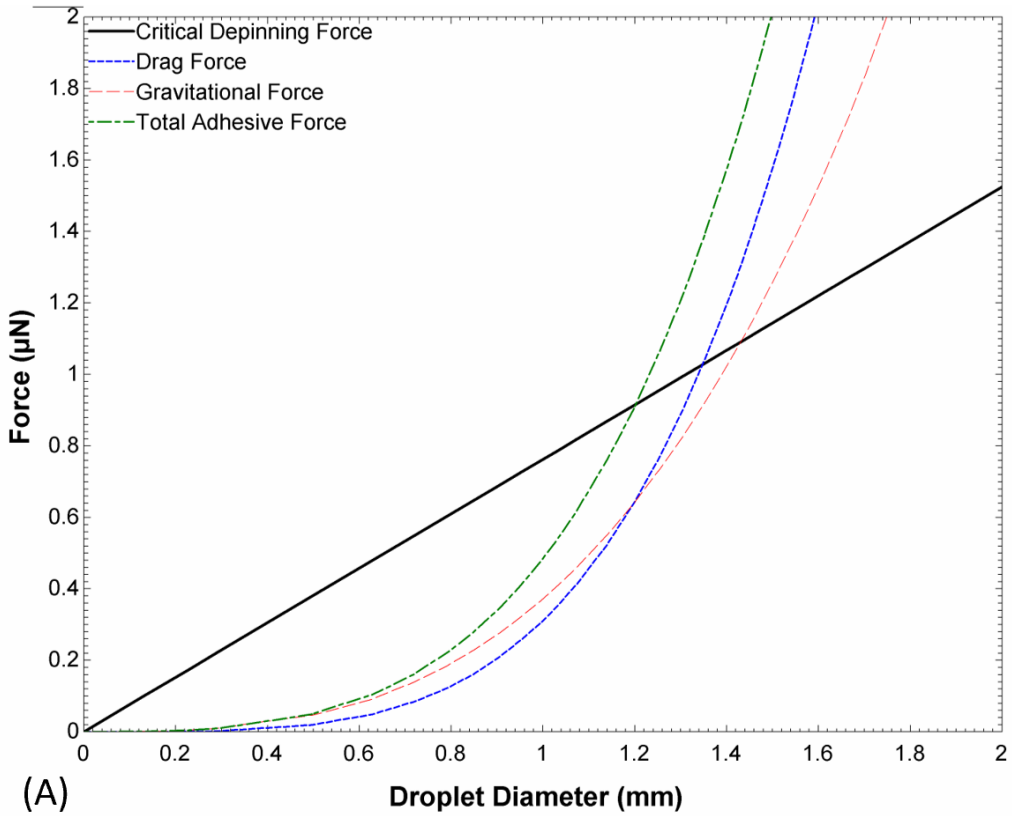

Figure 6.6 Forces acting on a stationary droplet for a mass flux of 125 kg/m^2 and a quality of (A) 0.3, (B) 0.8

6.5 Pressure drops

As with the hydrophilic coupons where standard and inverted orientations were evaluated, the difference between the orientations had little effect on the pressure drop, despite the visual difference in the condensate. For the standard orientation hydrophilic plain coupon with a mass flux of 50 kg/m^{2}s, the pressure drops ranged from 1.3 kPa to 5.6 kPa for qualities from 0.18 to 0.79 with the maximum measure pressure drop of 5.7 kPa occurring at a quality of 0.52. At a mass flux of 125 kg/m^{2}s, the pressure drops ranged from 6.0 kPa to 68 kPa for qualities from 0.20 to 0.78. When inverted, for the mass flux of 50 kg/m^{2}s pressure drops varied from 0.19 kPa to 0.69 kPa for qualities from 0.20 to 0.69. For the mass flux of 125 kg/m^{2}s, from 8.4 kPa to 74 kPa for qualities from 0.21 to 0.78. Though being hydrophobic typically lowers the pressure drop [12-14], in this case pressure drops in the hydrophobic coupon are slightly higher than in the hydrophilic coupon. That said, the greatest difference between the measured hydrophilic and hydrophobic pressure drops were below 10% with the greatest difference of 5.4 kPa occurring for a mass flux of 125 kg/m^{2}K and a quality of 0.79.

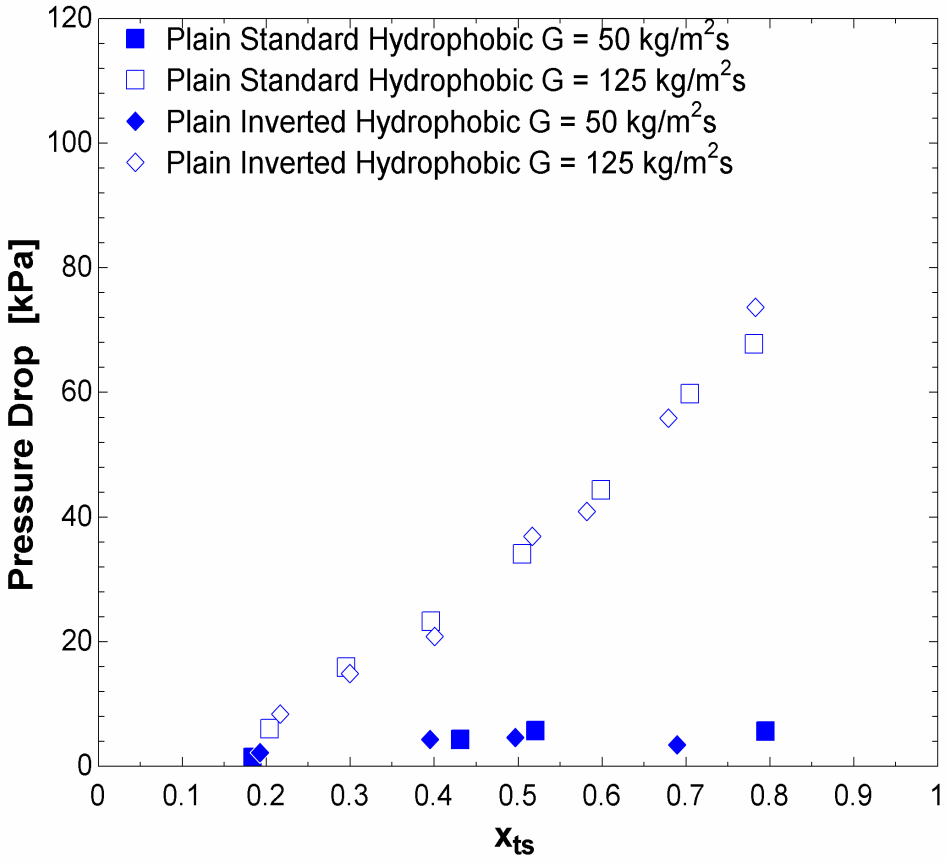

Figure 6.7 Pressure drops for the hydrophobic plain coupon in standard and inverted orientations

Chapter - 7 Conclusions and future work

An open-loop apparatus was utilized to measure the heat transfer coefficient and pressure drop, visualize, and change the orientation of the condensing surface of steam for mass fluxes of 50 kg/m^{2}s and 125 kg/m^{2}s and qualities from 0.2 to 0.9 at a pressure of 250 kPa. Test coupons had a hydraulic diameter of 1.9 mm and consisted of a plain coupon, a solid mound coupon, 100 µm and 200 µm monolayer coupons, and a 200 µm particle mound coupon. The plain and solid mound coupons were tested in both the standard and inverted orientation. The plain coupon was coated with Teflon AF^{TM}, to be hydrophobic and tested in both standard and inverted orientations. The following are the conclusions of this work.

Impacts of surface structures:

- Solid mounds enhanced the heat transfer coefficient from the plain coupon by a larger degree than the 13.8% larger surface area enhancement.
- For low qualities, $x < 0.4$, the presence of mounds forces the film to flow around them increasing the film velocity and thinning the film above the mound, thus increasing the heat transfer coefficient by up to 48% at a quality of 0.2 for both mass fluxes.
- For high qualities, $x < 0.6$, the mounds protrude through the film allowing for direct contact between them and the vapor, enhancing the heat transfer coefficient by up to 79% at a quality of 0.81 and a mass flux of 125 kg/m^{2}s.
- For the monolayer coupons, heat transfer coefficient enhancement was greatest for the 200 micron monolayer with a largest enhancement of 52% at a quality of 0.2 and a mass flux of 50 kg/m^{2}s. All other enhancements for the monolayer coupons were 22% or less, with negative enhancements occurring in both monolayers for the mass flux of 50 kg/m^{2}s.

- Particle sizes in the monolayers were not large enough to cause major film disruptions or consistently penetrate the liquid-vapor interface.
- While the 200 micron mound coupon had similar enhancement trends to the solid mound, heat transfer coefficient enhancement was lower in part due to smaller effective thermal conductivity of the sintered particle mounds.
- Due to laminar film conditions, the presence of micro-particles did not impact the pressure drops recorded. However, the mound coupons had higher pressure drops for all tested conditions.

Impacts of surface orientation:

- The inversion of hydrophilic coupons had minimal impact on either the heat transfer coefficients or flow patterns observed in the plain and solid mound coupons.
- Droplets in inverted hydrophobic coupons are smaller than those in the standard orientation. Droplet size reduction is most impacted by quality, though mass flux does also contribute. A droplet force model shows that maximum droplet size is decreased by as much as 13.5% for a quality of 0.2 and a mass flux of 50 kg/m^2s as compared to 1.8% for a 0.8 and a mass flux of 125 kg/m^2s.
- With the decreased maximum droplet size for the inverted hydrophobic coupon, heat transfer coefficients were also enhanced to a greater degree than when in the standard orientation. For a quality of 0.2 and mass flux of 50 kg/m^2s, the enhancement in standard orientation was 319% while in the inverted orientation the enhancement was 479% greater than the plain hydrophilic coupon in standard orientation.
- Orientation did not meaningfully impact pressure drop for any coupon evaluated.

Impacts of hydrophobicity:

- By coating the plain coupon in Teflon AF^{TM}, dropwise condensation was induced and observed with droplets being cleared from the condensing surface due to either shear forces or joining with a film rivulet flowing through the condensing surface.
- Standard orientation heat transfer coefficients were greatly improved via this mode of flow condensation, with the lowest enhancement of 190% occurring for a quality of 0.79 and mass flux of 50 kg/m^{2}s and a greatest enhancement 660% for a quality of 0.78 and mass flux of 125 kg/m^{2}s.
- Uncertainties for dropwise condensation are generally larger than those which occurred during filmwise condensation due to the high heat transfer coefficients and small difference in temperature between the steam and condensing surface, with a minimum temperature difference of 0.3 °C for a quality of 0.78 and mass flux of 125 kg/m^{2}s.

Future work from this research should include the following:

- Determining the effects of pin fin size and shape on film disruption and heat transfer coefficients.
- Determining the effects of fin placement, and frequency in an array on film distribution and heat transfer coefficients.
- Analyzing the effects of hydrophobic coatings on film and heat transfer coefficients when applied to the existing or new coupons with porous or solid surface structures.
- Further modeling the forces which lead to droplet depinning and experimentally verifying through high-speed videography and heat transfer measurements.

References

[1] G. A. Riley, C. E. Mendez, M. Egbo, G. Hwang, and M. M. Derby, "Visualizing and disrupting liquid films for filmwise flow condensation in horizontal minichannels," *Frontiers in Thermal Engineering,* vol. 2, p. 953051, 2022.

[2] J. Ho and K. Leong, "A critical review of filmwise natural and forced convection condensation on enhanced surfaces," *Applied Thermal Engineering,* vol. 186, p. 116437, 2021.

[3] I. Mudawar, "Flow boiling and flow condensation in reduced gravity," *Advances in Heat Transfer,* vol. 49, pp. 225-306, 2017.

[4] A. Berto, M. Azzolin, S. Bortolin, M. Miscevic, P. Lavieille, and D. Del Col, "Condensation heat transfer in microgravity conditions," *npj Microgravity,* vol. 9, p. 32, 2023.

[5] H. Jones, "The recent large reduction in space launch cost," 2018.

[6] J. Sun and H. S. Wang, "On the early and developed stages of surface condensation: competition mechanism between interfacial and condensate bulk thermal resistances," *Scientific reports,* vol. 6, pp. 1-12, 2016.

[7] D. Niu, L. Guo, H. Hu, and G. Tang, "Dropwise condensation heat transfer model considering the liquid-solid interfacial thermal resistance," *International Journal of Heat and Mass Transfer,* vol. 112, pp. 333-342, 2017.

[8] E. Alizadeh-Birjandi, A. Alshehri, and H. P. Kavehpour, "Condensation on Surfaces With Biphilic Topography: Experiment and Modeling," *Frontiers in Mechanical Engineering,* vol. 5, p. 38, 2019.

[9] X. Chen and M. M. Derby, "Combined visualization and heat transfer measurements for steam flow condensation in hydrophilic and hydrophobic mini-gaps," *Journal of Heat Transfer,* vol. 138, 2016.

[10] X. Ma, S. Wang, Z. Lan, A. Wang, and B. Peng, "Dropwise condensation heat transfer on superhydrophobic surface in the presence of non-condensable gas," in *Proceedings of the 14th International Heat Transfer Conference*, Washington, DC, 2010, pp. 71-79.

[11] D. Orejon, O. Shardt, N. S. K. Gunda, T. Ikuta, K. Takahashi, Y. Takata, *et al.*, "Simultaneous dropwise and filmwise condensation on hydrophilic microstructured surfaces," *International Journal of Heat and Mass Transfer,* vol. 114, pp. 187-197, 2017.

[12] B. El Fil, G. Kini, and S. Garimella, "A review of dropwise condensation: Theory, modeling, experiments, and applications," *International Journal of Heat and Mass Transfer,* vol. 160, p. 120172, 2020.

[13] J. Rose, "Dropwise condensation theory and experiment: a review," *Proceedings of the Institution of Mechanical Engineers, Part A: Journal of Power and Energy,* vol. 216, pp. 115-128, 2002.

[14] K. El Kadi, F. Alnaimat, and S. Sherif, "Recent advances in condensation heat transfer in mini and micro channels: A comprehensive review," *Applied Thermal Engineering,* vol. 197, p. 117412, 2021.

[15] D. H. Nguyen and H. S. Ahn, "A comprehensive review on micro/nanoscale surface modification techniques for heat transfer enhancement in heat exchanger," *International Journal of Heat and Mass Transfer,* vol. 178, p. 121601, 2021.

[16] S.-F. Zheng, U. Gross, and X.-D. Wang, "Dropwise condensation: From fundamentals of wetting, nucleation, and droplet mobility to performance improvement by advanced

functional surfaces," *Advances in Colloid and Interface Science,* vol. 295, p. 102503, 2021.
[17] A. S. Dalkilic and S. Wongwises, "Intensive literature review of condensation inside smooth and enhanced tubes," *International Journal of Heat and Mass Transfer,* vol. 52, pp. 3409-3426, 2009.
[18] A. Cavallini, G. Censi, D. Del Col, L. Doretti, G. Longo, L. Rossetto, *et al.*, "Condensation inside and outside smooth and enhanced tubes—a review of recent research," *International Journal of Refrigeration,* vol. 26, pp. 373-392, 2003.
[19] S.-M. Kim, J. Kim, and I. Mudawar, "Flow condensation in parallel micro-channels–Part 1: Experimental results and assessment of pressure drop correlations," *International journal of heat and mass transfer,* vol. 55, pp. 971-983, 2012.
[20] S.-M. Kim and I. Mudawar, "Flow condensation in parallel micro-channels–Part 2: Heat transfer results and correlation technique," *International Journal of Heat and Mass Transfer,* vol. 55, pp. 984-994, 2012.
[21] S.-M. Kim and I. Mudawar, "Universal approach to predicting heat transfer coefficient for condensing mini/micro-channel flow," *International Journal of Heat and Mass Transfer,* vol. 56, pp. 238-250, 2013.
[22] S.-M. Kim and I. Mudawar, "Universal approach to predicting two-phase frictional pressure drop for adiabatic and condensing mini/micro-channel flows," *International Journal of Heat and Mass Transfer,* vol. 55, pp. 3246-3261, 2012.
[23] D. W. Shao and E. G. Granryd, "Flow pattern, heat transfer and pressure drop in flow condensation part I: pure and azeotropic refrigerants," *HVAC&R Research,* vol. 6, pp. 175-195, 2000.
[24] M. Ahlers, A. Buck-Emden, and H.-J. Bart, "Is dropwise condensation feasible? A review on surface modifications for continuous dropwise condensation and a profitability analysis," *Journal of advanced research,* vol. 16, pp. 1-13, 2019.
[25] J. Dirker, D. Juggurnath, A. Kaya, E. A. Osowade, M. Simpson, S. Lecompte, *et al.*, "Thermal energy processes in direct steam generation solar systems: Boiling, condensation and energy storage–A review," *Frontiers in Energy Research,* vol. 6, p. 147, 2019.
[26] S. Lips and J. P. Meyer, "Two-phase flow in inclined tubes with specific reference to condensation: a review," *International Journal of Multiphase Flow,* vol. 37, pp. 845-859, 2011.
[27] L. E. O'Neill and I. Mudawar, "Review of two-phase flow instabilities in macro-and micro-channel systems," *International Journal of Heat and Mass Transfer,* vol. 157, p. 119738, 2020.
[28] J. Wen, X. Gu, Y. Liu, S. Wang, and Y. Li, "Effect of surface tension, gravity and turbulence on condensation patterns of R1234ze (E) in horizontal mini/macro-channels," *International Journal of Heat and Mass Transfer,* vol. 125, pp. 153-170, 2018.
[29] G. Qiu, M. Li, and W. Cai, "The condensation heat transfer, frictional pressure drop and refrigerant charge characteristics of R290 in minichannels with different diameters," *International Journal of Heat and Mass Transfer,* vol. 158, p. 119966, 2020.
[30] J. Wu, M. Shi, Y. Chen, and X. Li, "Visualization study of steam condensation in wide rectangular silicon microchannels," *International Journal of Thermal Sciences,* vol. 49, pp. 922-930, 2010.

[31] H. El Mghari, M. Asbik, H. Louahlia-Gualous, and I. Voicu, "Condensation heat transfer enhancement in a horizontal non-circular microchannel," *Applied Thermal Engineering*, vol. 64, pp. 358-370, 2014.
[32] H. El Mghari and H. Louahlia-Gualous, "Experimental and numerical investigations of local condensation heat transfer in a single square microchannel under variable heat flux," *International Communications in Heat and Mass Transfer*, vol. 71, pp. 197-207, 2016.
[33] M. Łukaszuk and T. Skiepko, "Condensation heat transfer coefficient during steam intermittent flows in a horizontal minichannel," *Experimental Thermal and Fluid Science*, vol. 145, p. 110875, 2023.
[34] H. Felcar, G. Ribatski, and J. S. Jabardo, "A gas-liquid flow pattern predictive method for macro-and-mini-scale round channels," in *Proc. 10th UK Heat Transfer Conference, Edinburgh, Scotland*, 2007.
[35] K. Cheng, S. Kim, S. Lee, and K. J. Kim, "Internal dropwise condensation: modeling and experimental framework for horizontal tube condensers," *International Journal of Heat and Mass Transfer*, vol. 83, pp. 99-108, 2015.
[36] D. E. Kim, H. S. Ahn, and T.-S. Kwon, "Experimental investigation of filmwise and dropwise condensation inside transparent circular tubes," *Applied Thermal Engineering*, vol. 110, pp. 412-423, 2017.
[37] X. Quan, P. Cheng, and H. Wu, "Transition from annular flow to plug/slug flow in condensation of steam in microchannels," *International Journal of Heat and Mass Transfer*, vol. 51, pp. 707-716, 2008.
[38] H. Soliman, "On the annular-to-wavy flow pattern transition during condensation inside horizontal tubes," *The Canadian Journal of Chemical Engineering*, vol. 60, pp. 475-481, 1982.
[39] M. Soliman, J. Schuster, and P. Berenson, "A general heat transfer correlation for annular flow condensation," 1968.
[40] S. G. Kandlikar and W. J. Grande, "Evolution of microchannel flow passages--thermohydraulic performance and fabrication technology," *Heat transfer engineering*, vol. 24, pp. 3-17, 2003.
[41] K. K. Bultongez and M. M. Derby, "Investigation of oil-water flow regimes and pressure drops in mini-channels," *International Journal of Multiphase Flow*, vol. 96, pp. 101-112, 2017.
[42] J. W. Coleman and S. Garimella, "Characterization of two-phase flow patterns in small diameter round and rectangular tubes," *International Journal of Heat and Mass Transfer*, vol. 42, pp. 2869-2881, 1999.
[43] T. Zhao and Q. Bi, "Co-current air–water two-phase flow patterns in vertical triangular microchannels," *International Journal of Multiphase Flow*, vol. 27, pp. 765-782, 2001.
[44] H. Ide, A. Kariyasaki, and T. Fukano, "Fundamental data on the gas–liquid two-phase flow in minichannels," *International Journal of Thermal Sciences*, vol. 46, pp. 519-530, 2007.
[45] H. Wu and P. Cheng, "Condensation flow patterns in silicon microchannels," *International Journal of Heat and Mass Transfer*, vol. 48, pp. 2186-2197, 2005.
[46] X. Ma, X. Fan, Z. Lan, and T. Hao, "Flow patterns and transition characteristics for steam condensation in silicon microchannels," *Journal of Micromechanics and Microengineering*, vol. 21, p. 075009, 2011.

[47] M. M. Derby, *Study of flow condensation enhancement with hydrophobic and hydrophilic patterns*: Rensselaer Polytechnic Institute, 2013.
[48] X. Chen, *Droplet dynamics in mini-channel steam flow condensation*: Kansas State University, 2017.
[49] A. K. Sadaghiani, "Numerical and experimental studies on flow condensation in hydrophilic microtubes," *Applied Thermal Engineering,* vol. 197, p. 117359, 2021.
[50] V. Khanikar, I. Mudawar, and T. S. Fisher, "Flow boiling in a micro-channel coated with carbon nanotubes," *IEEE Transactions on Components and Packaging Technologies,* vol. 32, pp. 639-649, 2009.
[51] X. Li, I. Cole, and J. Tu, "A review of nucleate boiling on nanoengineered surfaces–The nanostructures, phenomena and mechanisms," *International Journal of Heat and Mass Transfer,* vol. 141, pp. 20-33, 2019.
[52] G. Liang and I. Mudawar, "Review of nanoscale boiling enhancement techniques and proposed systematic testing strategy to ensure cooling reliability and repeatability," *Applied Thermal Engineering,* vol. 184, p. 115982, 2021.
[53] Y. Nasersharifi, M. Kaviany, and G. Hwang, "Pool-boiling enhancement using multilevel modulated wick," *Applied Thermal Engineering,* vol. 137, pp. 268-276, 2018.
[54] J. A. Weibel, S. V. Garimella, and M. T. North, "Characterization of evaporation and boiling from sintered powder wicks fed by capillary action," *International Journal of Heat and Mass Transfer,* vol. 53, pp. 4204-4215, 2010.
[55] S. N. R. Abadi, M. Mehrabi, and J. P. Meyer, "Numerical study of steam condensation inside a long, inclined, smooth tube at different saturation temperatures," *International Journal of Heat and Mass Transfer,* vol. 126, pp. 15-25, 2018.
[56] L. Zhang, S. Yang, and H. Xu, "Experimental study on condensation heat transfer characteristics of steam on horizontal twisted elliptical tubes," *Applied Energy,* vol. 97, pp. 881-887, 2012.
[57] X. Quan, L. Dong, and P. Cheng, "Determination of annular condensation heat transfer coefficient of steam in microchannels with trapezoidal cross sections," *International Journal of Heat and Mass Transfer,* vol. 53, pp. 3670-3676, 2010.
[58] H. Wang and J. W. Rose, "Film condensation in horizontal microchannels: effect of channel shape," in *International Conference on Nanochannels, Microchannels, and Minichannels*, 2005, pp. 729-735.
[59] T. Hao, X. Ma, Z. Lan, R. Jiang, and X. Fan, "Analysis of the transition from laminar annular flow to intermittent flow of steam condensation in noncircular microchannels," *International Journal of Heat and Mass Transfer,* vol. 66, pp. 745-756, 2013.
[60] J. Ho and K. Leong, "Filmwise condensation of steam on pin fin arrays fabricated by selective laser melting," in *Defect and Diffusion Forum*, 2019, pp. 71-82.
[61] X. Wang, J. Y. Ho, K. C. Leong, and T. N. Wong, "Condensation heat transfer and pressure drop characteristics of R-134a in horizontal smooth tubes and enhanced tubes fabricated by selective laser melting," *International Journal of Heat and Mass Transfer,* vol. 126, pp. 949-962, 2018.
[62] J. Royal and A. Bergles, "Augmentation of horizontal in-tube condensation by means of twisted-tape inserts and internally finned tubes," 1978.
[63] J. Ho, K. Leong, and T. Wong, "Forced convection condensation of R134a in three-dimensional conical pin fin tubes," *International Journal of Heat and Mass Transfer,* vol. 144, p. 118599, 2019.

[64] K. Aroonrat and S. Wongwises, "Experimental investigation of condensation heat transfer and pressure drop of R-134a flowing inside dimpled tubes with different dimpled depths," *International Journal of Heat and Mass Transfer,* vol. 128, pp. 783-793, 2019.
[65] S. Modak, M. Kaviany, S. Hoenig, and R. Bonner, "Numerical analysis of meniscus dynamics in monolayer-wick dropwise condensation," *Numerical Heat Transfer, Part A: Applications,* pp. 1-20, 2019.
[66] L. E. O'Neill, I. Park, C. R. Kharangate, V. Devahdhanush, V. Ganesan, and I. Mudawar, "Assessment of body force effects in flow condensation, part II: Criteria for negating influence of gravity," *International journal of heat and mass transfer,* vol. 106, pp. 313-328, 2017.
[67] I. Park, L. E. O'Neill, C. R. Kharangate, and I. Mudawar, "Assessment of body force effects in flow condensation, Part I: Experimental investigation of liquid film behavior for different orientations," *International journal of heat and mass transfer,* vol. 106, pp. 295-312, 2017.
[68] L. E. O'Neill, R. Balasubramaniam, H. K. Nahra, M. M. Hasan, and I. Mudawar, "Flow condensation heat transfer in a smooth tube at different orientations: Experimental results and predictive models," *International Journal of Heat and Mass Transfer,* vol. 140, pp. 533-563, 2019.
[69] A. Faghri and L. Chow, "Forced condensation in a tube with suction at the wall for microgravitational applications," 1988.
[70] X. Chen, J. A. Morrow, and M. M. Derby, "Mini-channel flow condensation enhancement through hydrophobicity in the presence of noncondensable gas," *International Journal of Heat and Mass Transfer,* vol. 115, pp. 11-18, 2017.
[71] D. S. Antao, K. L. Wilke, J. H. Sack, Z. Xu, D. J. Preston, and E. N. Wang, "Jumping droplet condensation in internal convective vapor flow," *International Journal of Heat and Mass Transfer,* vol. 163, p. 120398, 2020.
[72] N. Miljkovic and E. N. Wang, "Condensation heat transfer on superhydrophobic surfaces," *MRS bulletin,* vol. 38, pp. 397-406, 2013.
[73] M. J. Hoque, S. Chavan, R. Lundy, L. Li, J. Ma, X. Yan, *et al.*, "Biphilic jumping-droplet condensation," *Cell Reports Physical Science,* vol. 3, p. 100823, 2022.
[74] M. Kedzierski and J. Worthington III, "Design and machining of copper specimens with micro holes for accurate heat transfer measurements," *EXPERIMENTAL HEAT TRANSFER An International Journal,* vol. 6, pp. 329-344, 1993.
[75] Y. Muzychka and M. Yovanovich, "Laminar forced convection heat transfer in the combined entry region of non-circular ducts," *J. Heat Transfer,* vol. 126, pp. 54-61, 2004.
[76] J. Ho and K. Leong, "Effect of fin pitch on the filmwise condensation of steam on three-dimensional conical pin fin arrays: A comparative study," *International Journal of Heat and Mass Transfer,* vol. 150, p. 119328, 2020.
[77] D. Butterworth, "A comparison of some void-fraction relationships for co-current gas-liquid flow," *International Journal of Multiphase Flow,* vol. 1, pp. 845-850, 1975.
[78] I. V. Roisman, A. Criscione, C. Tropea, D. K. Mandal, and A. Amirfazli, "Dislodging a sessile drop by a high-Reynolds-number shear flow at subfreezing temperatures," *Physical Review E,* vol. 92, p. 023007, 2015.

Appendix A Condensation Data

Table 7.1 Plain hydrophilic coupon in standard orientation

G (kg/m^2s)	x_{ts}	ω_{xts}	Δx	h_{plan} (W/m^2K)	ω_h (W/m^2K)	q" (W/m^2)	T_{fluid} (°C)	T_{wall} (°C)	ΔP (kPa)
50.3	0.2014	0.0131	0.1840	22173	1273	363782	127.9	111.5	1.8
51.0	0.4094	0.0097	0.1963	33317	2123	393581	127.8	115.9	3.2
51.1	0.5932	0.0842	0.2105	42909	2964	423439	127.6	117.8	4.7
50.4	0.7944	0.0051	0.2115	47494	3533	419476	127.5	118.7	5.9
49.9	0.8686	0.0057	0.2922	52997	2991	631088	127.0	115.1	8.8
124.5	0.3289	0.0104	0.0948	40757	2470	475860	128.0	116.3	15.0
124.6	0.3926	0.0093	0.0947	44607	2832	480261	127.6	116.8	20.1
125.9	0.5033	0.0076	0.0929	50986	3508	483936	126.8	117.3	30.3
125.2	0.5989	0.0061	0.0927	57104	4231	487079	126.3	117.7	40.8
125.9	0.6987	0.0046	0.0878	65243	5478	473997	124.5	117.2	54.3
124.9	0.7928	0.0033	0.0884	71055	6381	474159	124.0	117.3	61.5
124.3	0.9744	0.0017	0.0687	95177	10818	480278	121.4	116.4	91.6

Table 7.2 100 µm monolayer hydrophilic coupon in standard orientation

G (kg/m^2s)	x_{ts}	ω_{xts}	Δx	$h_{planform}$ (W/m^2K)	ω_h (W/m^2K)	q" (W/m^2)	T_{fluid} (°C)	T_{wall} (°C)	ΔP (kPa)
50.3	0.1977	0.0127	0.2237	26183	1362	442730	127.6	110.7	1.3
49.9	0.3956	0.0096	0.2328	29981	1608	456735	127.4	112.2	3.2
50.0	0.5915	0.0069	0.2416	38094	2224	475513	127.3	114.8	4.7
50.6	0.8135	0.0392	0.2540	47197	2972	505708	127.1	116.3	6.9
125.3	0.3703	0.0095	0.0962	49251	3270	490988	127.1	117.2	20.3
127.0	0.4033	0.0090	0.0932	51621	3573	485404	126.8	117.4	24.2
124.9	0.4998	0.0075	0.0957	56219	4066	494134	126.5	117.7	30.5
126.7	0.5998	0.0059	0.0925	63140	4986	493107	125.5	117.7	42.4
125.2	0.7086	0.0043	0.0933	70212	5979	497116	124.7	117.6	53.6
124.3	0.7924	0.0032	0.0923	75418	6871	492025	123.9	117.4	63.0

Table 7.3 200 µm monolayer hydrophilic coupon in standard orientation

G (kg/m^2s)	x_{ts}	ω_{xts}	Δx	$h_{planform}$ (W/m^2K)	ω_h (W/m^2K)	q" (W/m^2)	T_{fluid} (°C)	T_{wall} (°C)	ΔP (kPa)
51.1	0.1984	0.0128	0.2270	33305	1876	456349	127.9	114.2	0.9
50.7	0.3968	0.0098	0.2303	37124	2201	459052	127.8	115.4	2.0
50.2	0.5836	0.0832	0.2532	43694	2649	499681	127.7	116.3	3.8
50.3	0.7937	0.0052	0.2411	47409	3148	476897	127.5	117.5	4.8
50.3	0.9017	0.0051	0.2321	65546	4992	529886	127.3	119.2	8.9
125.2	0.3267	0.0103	0.0994	45990	2874	500428	127.7	116.8	14.4
124.5	0.3994	0.0091	0.0999	50462	3323	504969	127.3	117.3	20.3
124.5	0.5064	0.0074	0.0979	57876	4200	504175	126.5	117.8	32.1
125.2	0.6002	0.0060	0.0948	66467	5390	500287	125.1	117.6	44.5
126.3	0.7007	0.0045	0.0954	71437	5971	515061	124.4	117.2	55.6
125.3	0.7958	0.0032	0.0950	77675	6985	512204	123.7	117.1	65.7
123.9	0.9745	0.0018	0.0712	100388	11486	501141	121.8	116.8	87.7

Table 7.4 Solid mound hydrophilic coupon in standard orientation

G (kg/m^2s)	x_{ts}	ω_{xts}	Δx	$h_{planform}$ (W/m^2K)	ω_h (W/m^2K)	q" (W/m^2)	T_{fluid} (°C)	T_{wall} (°C)	ΔP (kPa)
51.5	0.2081	0.0125	0.2006	33519	1754	363691	127.7	115.3	1.2
51.4	0.4105	0.0095	0.1807	48077	3455	328052	127.6	119.8	4.9
51.4	0.6183	0.0779	0.2107	57872	4148	382926	127.2	119.6	7.7
51.4	0.8117	0.0585	0.2110	59832	4396	383329	127.1	119.8	9.2
127.0	0.1997	0.0123	0.0793	44371	2751	363568	127.9	118.6	10.1
126.0	0.2993	0.0107	0.0795	51236	3469	368659	127.3	119.1	18.3
124.2	0.4361	0.0086	0.0816	59456	4285	389426	125.6	118.2	39.1
124.5	0.4978	0.0077	0.0811	61594	4553	390355	125.4	118.2	43.9
123.0	0.6022	0.0061	0.0784	69202	5662	387108	123.7	117.4	63.4
126.7	0.7038	0.0045	0.0687	87045	9021	371082	121.5	116.7	87.4
125.3	0.8082	0.0030	0.0646	131732	20373	363744	119.4	116.2	114.0

Table 7.5 200 µm mound hydrophilic coupon in standard orientation

G (kg/m^2s)	x_{ts}	ω_{xts}	Δx	$h_{planform}$ (W/m^2K)	ω_h (W/m^2K)	q" (W/m^2)	T_{fluid} (°C)	T_{wall} (°C)	ΔP (kPa)
50.7	0.2090	0.0124	0.2337	35305	1699	417185	127.8	114.4	3.1
50.3	0.4004	0.0094	0.2362	41757	2206	418864	127.7	116.3	4.8
51.5	0.4535	0.0087	0.2317	41921	2209	421400	127.5	116.0	5.4
50.7	0.7074	0.0057	0.2366	42996	2296	422470	127.7	116.5	5.4
51.8	0.8091	0.0048	0.2351	50556	2962	429879	127.2	117.5	8.6
125.1	0.2076	0.0122	0.0892	37292	1904	402434	127.9	115.6	10.7
126.0	0.3066	0.0106	0.0908	44682	2464	418748	127.2	116.6	18.6
125.8	0.4043	0.0091	0.0893	53262	3298	420836	126.4	117.5	29.6
124.6	0.5010	0.0075	0.0894	59886	4004	425828	125.6	117.5	42.5
124.8	0.5968	0.0964	0.0850	64293	4631	416827	124.4	117.0	57.8
125.8	0.6982	0.0703	0.0822	73283	5819	420806	122.7	116.2	79.4
124.8	0.7902	0.0032	0.0815	78943	6672	420888	121.5	115.4	95.2

Table 7.6 Plain hydrophilic coupon in inverted orientation

G (kg/m^2s)	x_{ts}	ω_{xts}	Δx	$h_{planform}$ (W/m^2K)	ω_h (W/m^2K)	q" (W/m^2)	T_{fluid} (°C)	T_{wall} (°C)	ΔP (kPa)
49.3	0.2039	0.0127	0.2155	23705	1245	417887	127.4	109.8	1.8
51.8	0.4069	0.0095	0.2177	31713	1784	444008	127.2	113.2	3.4
53.0	0.4950	0.1065	0.2191	35567	2070	456645	127.2	114.4	4.4
49.0	0.8714	0.0052	0.2666	47020	2836	530714	126.8	115.5	9.9
123.8	0.3379	0.0102	0.0909	37280	2232	454912	126.7	114.5	16.2
126.1	0.4163	0.0089	0.0890	43951	2870	459829	126.0	115.6	22.3
127.5	0.5080	0.0074	0.0871	50492	3563	466581	125.7	116.4	37.1
126.1	0.6001	0.0061	0.0854	53356	3987	456732	125.2	116.7	43.2
126.4	0.6946	0.0046	0.0829	58705	4693	457840	123.0	115.2	60.7
123.5	0.7946	0.0459	0.0849	62040	5170	457973	122.6	115.3	66.9

Table 7.7 Solid mound hydrophilic coupon in inverted orientation

G (kg/m^2s)	x_{ts}	ω_{xts}	Δx	$h_{planform}$ (W/m^2K)	ω_h (W/m^2K)	q" (W/m^2)	T_{fluid} (°C)	T_{wall} (°C)	ΔP (kPa)
50.5	0.2288	0.0119	0.2070	37263	2044	368955	127.1	115.8	3.1
49.5	0.3923	0.0095	0.2189	47430	2938	383245	127.0	117.8	5.8
49.5	0.5616	0.0877	0.2230	55299	3764	390298	126.8	118.7	8.4
50.7	0.8964	0.0043	0.2140	74763	6360	397853	126.2	120.1	17.6
125.7	0.2076	0.0116	0.0801	42251	2530	364625	127.9	118.1	11.1
127.2	0.3150	0.0104	0.0794	52036	3519	373882	127.1	118.9	20.6
124.1	0.3980	0.0091	0.0804	57994	4234	375860	126.9	119.5	29.6
124.3	0.5057	0.0074	0.0807	66853	5269	390939	124.8	118.1	46.9
126.2	0.6120	0.0057	0.0753	73830	6413	384750	123.3	117.4	65.1
125.1	0.6907	0.0046	0.0685	83430	8514	362666	122.3	117.3	84.3
125.7	0.8032	0.0030	0.0646	110127	14323	365764	119.5	115.8	115.6

Table 7.8 Plain hydrophobic coupon in standard orientation

G (kg/m^2s)	x_{ts}	ω_{xts}	Δx	$h_{planform}$ (W/m^2K)	ω_h (W/m^2K)	q" (W/m^2)	T_{fluid} (°C)	T_{wall} (°C)	ΔP (kPa)
52.0	0.1833	0.0134	0.1132	86560	18310	232527	128.0	125.3	1.4
50.9	0.4311	0.0096	0.0868	125153	49553	174516	127.8	126.4	4.3
50.2	0.5206	0.0083	0.0857	142334	65451	169933	127.7	126.5	5.7
49.6	0.7948	0.0050	0.0815	141939	69318	159554	127.7	126.5	5.6
122.8	0.2036	0.0128	0.0298	109802	44791	149588	127.5	126.1	6.1
122.5	0.2950	0.0113	0.0288	163220	96128	151426	126.8	125.8	15.9
126.1	0.3960	0.0097	0.0260	165146	99616	149540	126.1	125.2	23.3
124.9	0.5046	0.0080	0.0243	206770	157777	147253	125.3	124.6	34.1
123.2	0.5984	0.1049	0.0231	252447	237051	145661	124.6	124.0	44.3
126.1	0.7045	0.0046	0.0233	344922	401913	159936	123.0	122.6	59.8
126.8	0.7808	0.0039	0.0236	536446	961423	161411	124.3	124.0	67.8

Table 7.9 Plain hydrophobic coupon in inverted orientation

G (kg/m^2s)	x_{ts}	ω_{xts}	Δx	$h_{planform}$ (W/m^2K)	ω_h (W/m^2K)	q" (W/m^2)	T_{fluid} (°C)	T_{wall} (°C)	ΔP (kPa)
48.3	0.1924	0.0132	0.1515	123656	29386	288433	128.0	125.7	2.2
54.2	0.3950	0.0098	0.1370	153199	44003	292776	127.6	125.7	4.3
51.0	0.4963	0.0084	0.1473	158207	46373	295949	127.8	125.9	4.6
48.3	0.6895	0.1326	0.1560	143798	38364	296646	128.0	125.9	3.4
125.0	0.2163	0.0125	0.0534	174991	61917	270170	126.7	125.2	8.4
127.3	0.2991	0.0111	0.0522	197349	77403	274052	126.9	125.5	14.9
123.8	0.4003	0.0095	0.0528	213218	90189	274106	126.7	125.4	20.8
128.5	0.5167	0.0076	0.0477	334502	222434	271968	125.3	124.5	36.9
125.7	0.5814	0.0066	0.0448	404321	348616	253196	125.1	124.5	40.9
124.2	0.6791	0.0051	0.0456	412367	345958	265380	122.9	122.2	55.9
128.5	0.7828	0.0036	0.0401	773657	1266000	254797	122.4	122.1	73.7